Rapid microglial phenotype changes modulate neuronal networks and sharp wave-ripple activity in acute slice preparations

Authors

Péter Berki[1,3], Csaba Cserép[2], Balázs Pósfai[1,2], Eszter Szabadits[2], Zsuzsanna Környei[2], Anna Kellermayer[2], Miklós Nyerges[2], Attila I. Gulyás[3] and Ádám Dénes[2,*]

[1] János Szentágothai Doctoral School of Neuroscience, Semmelweis University, Budapest, H-1083 Hungary

[2] Momentum Laboratory of Neuroimmunology, Institute of Experimental Medicine, Budapest, H-1083 Hungary

[3] Laboratory of Cerebral Cortex Research, Institute of Experimental Medicine, Budapest, H-1083 Hungary

[*] Correspondence: denes.adam@koki.hu

Short title: Microglia modulate neuronal networks in acute slices

Abstract

Microglia, the main immune cells of the central nervous system (CNS) have long been known for their remarkable sensitivity to tissue disturbance or injury, but its implications to the interpretation of results from *ex vivo* models of the CNS have remained largely unclear to date. To this end, we have followed the course of microglial phenotype changes and contribution to neuronal network organisation and functioning in acute brain slices prepared from mice, widely used to study the physiology of the brain from nanoscale events to complex circuits. We found that upon acute slice preparation, microglial cell bodies dislocate and migrate towards the surface of slices, alongside with rapidly progressing morphological changes and altered interactions with neurons. This is accompanied by gradual depolarization and downregulation of P2Y12 receptors, which are instrumental for microglia-neuron communication. Quantitative post-embedding immunofluorescent labelling reveals time-dependent increase in the number of excitatory and inhibitory synapses upon slice preparation in the cerebral cortex, which are markedly influenced by microglia. In line with this, the absence of microglia diminishes the incidence, amplitude and frequency of sharp wave-ripple activity in hippocampal slices. Collectively, our data suggest that microglia are not only inherent modulators of complex neuronal networks, but their specific actions on network reorganisation and functioning must be taken into account when learning lessons from *ex vivo* models of the CNS.

Introduction

Since its first applications several decades ago (Andersen, 1981; Yamamoto & McIlwain, 1966), the acute brain slice preparation technique has become an instrumental tool in the field of neuroscience and have extensively contributed to our understanding of cellular physiology. As the methodology of slice preparation went through numerous iterations over the years (Brahma et al., 2000; Richerson & Messer, 1995; Ting et al., 2014), improvements have led to acute slices even capable of producing spontaneous oscillations, similar to those observed *in vivo* (Hájos et al., 2013; Mann et al., 2005; Perumal et al., 2021; Wu et al., 2005). Meanwhile, *ex vivo* studies of non-neuronal cell types such as astrocytes and microglia have also been emerging (Kettenmann et al., 2011; Verkhratsky & Nedergaard, 2018), alongside with increasing focus on bidirectional communication between neurons and glial cells (Eyo & Wu, 2013; Pannasch & Rouach, 2013). Microglia are the resident immunocompetent cells in the nervous system, with essential roles beyond their immune function under both physiological and pathological conditions (Masuda et al., 2020; Prinz et al., 2019). Because microglia are heavily involved in brain development and maintenance of neuronal populations (Kierdorf & Prinz, 2017; Thion et al., 2018), as well as their functional alterations are linked to a wide range of human diseases (Salter & Stevens, 2017; Song & Colonna, 2018; Wang & Colonna, 2019), interest in understanding microglial function has substantially increased over the last decade. As such, acute slice preparations also proved to be an essential tool for the investigation of microglia, since robust transcriptomic, proteomic and functional differences have been revealed between cultured and acute microglia properties (Boucsein et al., 2000, 2003; Butovsky et al., 2014; Färber & Kettenmann, 2005; Hellwig et al., 2013; Kettenmann et al., 2011; Melief et al., 2012; Schilling & Eder, 2007a; Schmid et al., 2009). In fact, the microglial gene expression profile is altered within minutes to hours of being in culture, as demonstrated by the downregulation of various important homeostatic genes

(e.g.: Tmem119, P2ry12, THIK, NKCC1), whereas acute slice preparations have been suggested to better preserve a microglial phenotype resembling that seen under physiological states (Bennett et al., 2018; Bohlen et al., 2017; Butovsky et al., 2014; Gosselin et al., 2017; Izquierdo et al., 2019). However, it is also acknowledged that microglia can rapidly become reactive in slices and translate to an amoeboid phenotype (Haynes et al., 2006; Petersen & Dailey, 2004; Stence et al., 2001). Importantly, while the acute slice technique have contributed with major advancements to microglia physiology (Boucsein et al., 2000; Färber & Kettenmann, 2005; Kettenmann et al., 2011; Schilling et al., 2000; Schilling & Eder, 2007b), the sensitivity of microglia to the slice preparation procedure and the impact of methodological practices that are essential for optimal electrophysiological measurements have remained vaguely characterized. This may be particularly important in light of the remarkable sensitivity of microglia to even subtle changes in their microenvironment (Hirbec et al., 2019; Masuda et al., 2020). A further unexplored territory is how microglia may influence complex neuronal circuits and their reorganization via time-dependent changes upon acute slice preparation. To this end, we set out to investigate microglia and the neuronal network simultaneously in slice preparations using an experimentally relevant timeframe. Our results suggest that microglia are inherent contributors for basic features of neuronal networks in acute slice preparations, which is remarkably influenced by microglial phenotype changes due to the slice preparation and incubation procedure. We suggest that these observations may be of high importance for both microglial and neuronal studies applying the acute brain slice technique.

Results

Microglia gradually migrate towards the surface of acute slice preparations

Microglia are well known to react rapidly to injury or tissue disturbance in the brain parenchyma (Davalos et al., 2005; Nimmerjahn et al., 2005). This is characterized by extension of their highly motile processes towards the injury site, which may be followed by translocation of their cell body depending on the nature and the extent of the insult. To investigate how injury caused by acute slice preparation influences microglia functions on a population level, we first tracked microglial cell body and process distribution during a 5 hour incubation period in 300 µm thick acute hippocampal slices from CX3CR1$^{+/GFP}$ microglia reporter mice (p.n.:~35 days). We consistently used a strictly controlled preparation and incubation procedure across all measurements (see details in Methods), which has been optimized for studying neuronal network dynamics, as slices prepared with this method are able to produce sharp wave-ripple activity (SWR) spontaneously (Hájos et al., 2013; Schlingloff et al., 2014). To monitor time dependent changes, slices were immersion-fixed at different time points after cutting (Figure 1A). Subsequently, preparations were resliced to obtain cross-sections and mounted onto glass plates for analysis (Figure 1B). Only the native microglial GFP signal was imaged via confocal laser-scanning microscopy, to avoid artefacts that might occur due to antibody penetration issues during immunofluorescent labelling. Original images were masked in order to display cell bodies or processes only, and a virtual grid was used to quantify distribution changes along the top to bottom axis of slice preparations (Figure 1C).

We found that translocation of microglial cell bodies occurs rapidly after slice preparation with most extensive changes in the top region (~40 µm) of slices (Figure 1D). Here, the density of cell bodies gradually increased by 75% throughout the 5 hours of the incubation (independent t-test, $p<0.01$), and reached significance at 42% ($p<0.05$) as early as 2 hours of

incubation (Figure 1E; blue). We also observed a decreasing trend of cell body density in the bottom region of slices, which started to increase again after 2 hours of incubation (Figure 1E; green, n.s.). Top region of slices showed a 42% higher density of cell bodies when compared to the bottom region (independent t-test, $p<0.01$) already after 2 hours of incubation (Figure 1E, black statistical indication). Since the gradually increasing density of cell bodies towards the top region suggested a displacement of cells during the incubation process, we decided to quantify these changes. To this end, we calculated the lowest distance of cell displacement in order to reach the 5 hours distribution starting from the 0 minute distribution (Figure 1F). Our results show that the translocation of cell bodies is a composite of two effects: a stronger effect acting in the direction of the top surface (median displacement from the bottom of the slice: 17,08 µm) and a smaller effect acting towards the top and bottom cut surfaces away from the middle of the slices (7,99 µm from the middle). The total number of microglia located in whole cross sections did not differ significantly during the course of the experiment (43.07 cells/grid at 0 min, 41.50 cells/grid at 5 hours; $p=0.788$), suggesting that microglia loss does not contribute substantially to the observed changes in cell distribution.

In line with this, the spatial distribution of microglial processes within the slice showed similar, but even more pronounced alterations during the course of the incubation process (Figure 1G). We observed that the percentage of the fluorescent signal corresponding to microglial processes in the top layer increased significantly by 21% ($p<0.05$) as early as 2 hours of incubation and by 29% ($p<0.001$) after 5 hours of incubation (Figure 1H, blue). Contrary to microglial cell bodies, process density at the bottom layer showed a significant drop by 15% ($p<0.05$) already after 2 hours of incubation (Figure 1H, green). Here, we also observed 23% ($p<0.05$) lower process density at the bottom region of slices compared to top after 5 hours of incubation (Figure 1H; black statistical indication, independent t-test). Importantly, the total

109 percentage of area covered by microglial processes dropped to half between the 0 minute and
110 5 hour time points ($p<0.0001$, independent t-test, Figure 1I).

111 To capture these changes in real time, slice preparations were transferred into a
112 recording chamber for confocal imaging (Figure 1J). The native signal of microglia
113 ($CX3CR1^{+/GFP}$) was continuously imaged for at least 6 hours after slice preparation (Figure 1K,
114 Supplementary Video 1-2). We found that individual cell behaviours correlated with the
115 quantitative data (Figure 1E-F, H-I), as we saw both processes and the cell body of microglia
116 (Figure 1K, coloured dots) express directed movement towards the top surface of slices (Figure
117 1K, white stripped line).

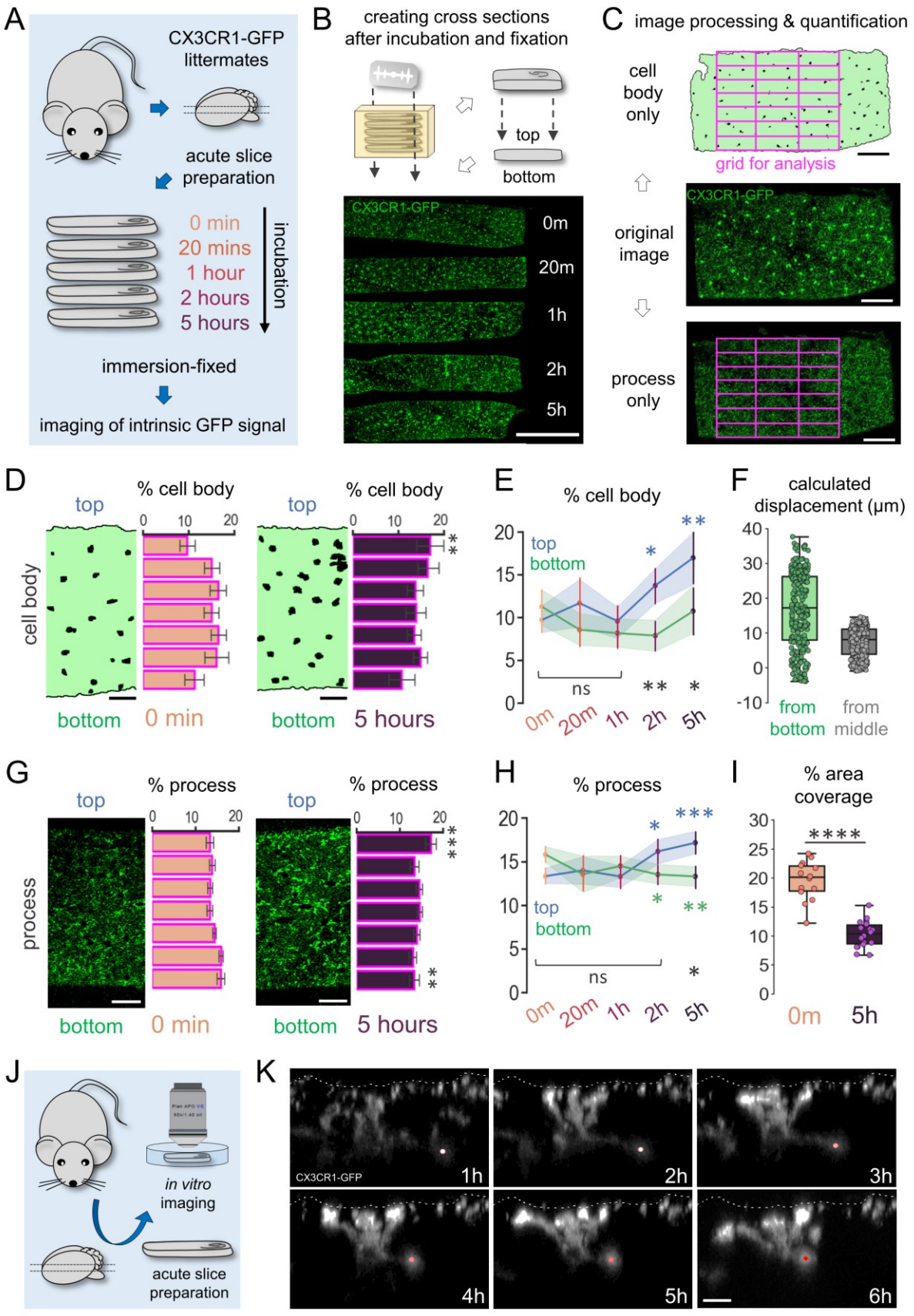

Figure 1. Microglia gradually migrate towards the surface of acute slice preparations

A. Schematic representation of the experiment. CX3CR1$^{+/GFP}$ littermates (N=3; p.n.: ~35 days) were used to create acute hippocampal slice preparations and placed into an interface-type incubation chamber for recovery. Slices were immersion-fixed immediately (0 minute) or after 20 minutes, 1 hour, 2 hours or 5 hours of incubation.

B. Cross sections were made from slice preparations that were fixed at different time points (top). Maximum intensity projection image shows cross-sections of slices mounted onto glass plates while preserving their top and bottom directionality according to their position in the incubation chamber. Native GFP signal of microglia were imaged via confocal laser-scanning microscopy (bottom, bar: 500 µm).

C. Original images were further processed (to contain either cell bodies or processes) and a 7x3 grid (violet) was used consequently for the quantification of cell body or process distributions along the grid layers (bar: 100 µm).

D. Representative sections of processed images at 0 minute and 5 hours showing distribution of microglial cell bodies along the top and bottom axis of slices (left, bar: 50 µm). Bar-plots are showing percentages of total cell bodies counted respective to the layers of the analysis grid (right). N=3, 3 slices/animal, mean ± SEM, independent t-test, **: p<0.01.

E. Line-plots representing measured changes of microglial cell body percentages across different time points within the top (blue) and bottom (green) layers of acute slice preparations. N=3, 3 slices/animal, median ± SEM, independent t-test, ns: not significant, *: p<0.05, **: p<0.01. Blue statistical indications show significant changes compared to 0 minute time point, black statistical indications compare top and bottom means at each time point.

F. Cell body translocation quantified as displacement (µm) towards the top measured from bottom (green) or middle (grey). N=3, p.n.: ~35 days; 3 slices/animal.

G. Same as in D) respective to microglial process fluorescence intensity calculated for each layer in the grid, mean ± SEM, independent t-test, **: p<0.01, ***: p<0.001.

H. Same as in E) respective to microglial process fluorescence intensity. N=3, p.n.: ~35 days; 3 slices/animal; mean ± SEM, independent t-test, ns: not significant, *: p<0.05, **: p<0.01, ***: p<0.001.

I. Percent of area covered by processes at the 0 minute and 5 hour time points, independent t-test, ****: p<0.001.

J. CX3CR1$^{+/GFP}$ mice (p.n.:45-80 days) were used to create acute hippocampal slices and transferred into a recording chamber for confocal or 2P imaging after cutting.

K. Extracted timeframes from Supplementary Video 1. Images show the translocation of microglial processes and the cell body towards the surface of slice preparations (white stripped line). Scale bar: 10 µm.

Microglia undergo rapid, progressive morphological changes in acute slices

Microglial cells are well known to retract their processes as an early response to injury and translate into an amoeboid, reactive phenotype. (Haynes et al., 2006; Petersen & Dailey, 2004; Stence et al., 2001). Our results on the decrease in area covered by microglial processes after 5 hours (Figure 1I) suggested robust changes in microglia morphology taking place in acute slice preparations. This behaviour was also evident in the data gathered by our imaging experiments, where we saw rapid transformation of individual microglial cells into a reactive phenotype (Figure 2A, Supplementary Video 3). To define the spatio-temporal characteristics of these pronounced morphological changes, preparations were immersion-fixed at different time points during incubation. In parallel, a group of mice were transcardially perfused to obtain slice preparations from the same region as controls (Figure 2B). Confocal images were analysed with a recently developed automated morphological analysis tool (Figure 2C; Heindl et al., 2018).

Confocal stacks showed drastic morphological differences in microglia induced by slice preparation. We observed rapid retraction of processes already visible in maximum intensity projection images created from the analysed z-stacks (Figure 2D), as well as on individual cell morphologies and skeleton reconstructions via the analysis tool (Figure 2E; Supplementary Video 4). Sphericity values of individual cells (measuring how amoeboid-like a cell is, where retraction of processes translate to higher sphericity values) increased by ~50% on average already after 20 minutes of incubation (independent t-test, $p<0.0001$), and peaked at ~100% increase ($p<0.0001$) between 1 and 2 hours of incubation both in regions of the cortex and in the hippocampus (Figure 2F). At the same time, total number of process endings dropped by ~50% after 20 minutes of incubation ($p<0.0001$), and this reduction also peaked between 1-2 hours of incubation with ~80% decrease in average (Figure 2G, $p<0.0001$). We also conducted

this experiment in an older group of animals (p.n.: ~95), and observed the same extensive changes concerning both cortical and hippocampal regions (Supplementary Figure 1).

In comparison with other studies, microglia after 1 hour of incubation showed extremely similar morphological characteristics (sphericity and numbers of process endings) to cells measured at peri-infarct cortical areas in experimental stroke models of mice (Morrison & Filosa, 2013; Sadler et al., 2020; Singh et al., 2018). Moreover, difference in the number of process endings observed in a study comparing control and Alzheimer's disease patients' microglial morphology (Davies et al., 2017) closely resemble the changes that we observed (~50% drop) after 20 minutes of incubation. Based on these observations, we concluded that microglia showed rapid morphological changes in acute slice preparations.

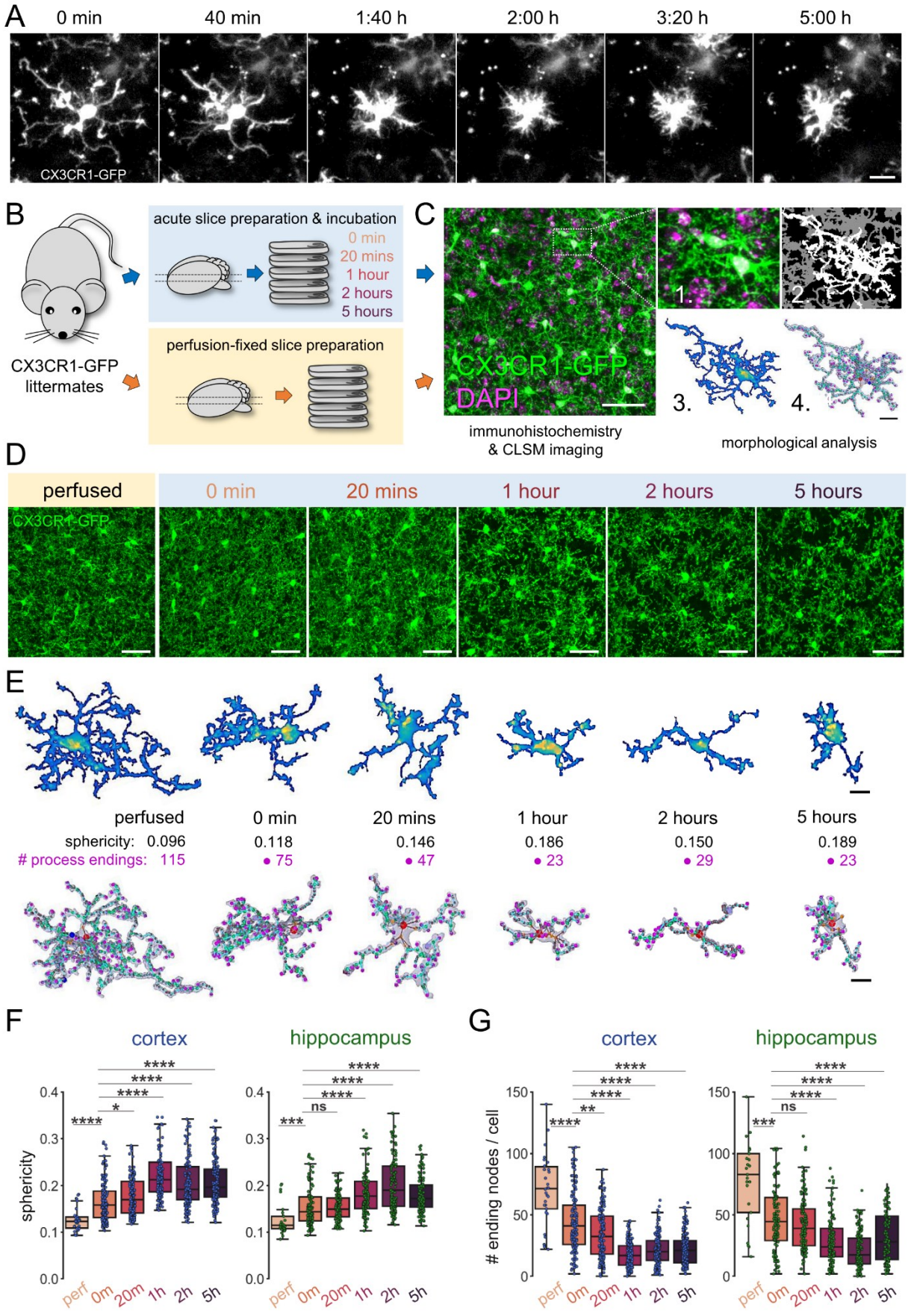

Figure 2. Microglia undergo rapid, progressive morphological changes in acute slices

A. Extracted timeframes from Supplementary Video 3. CX3CR1$^{+/GFP}$ signal of a single microglial cell was captured via confocal imaging at different time points after acute slice preparation. Scale bar: 10 µm.

B. Schematic representation of experiment. CX3CR1$^{+/GFP}$ littermates (N=8; p.n.: ~35 days) were used either to create hippocampal slice preparations, which were immersion-fixed before (0 minute) and after 20 minutes, 1 hour, 2 hours or 5 hours of incubation (blue arrows), or animals were perfusion fixed to obtain slice preparations with the same dimensions as acute slices (red arrows).

C. Slices were stained and z-stack images were obtained via confocal laser-scanning microscopy (left, bar: 20 µm). Images were analysed with an automated morphological analysis tool (Heindl et al, 2018) which uses raw z-stacks (1.) to isolate and segment the images to separate microglial cells (2.). Separate cells are further segmented (3.) to cell body (yellow) and processes (blue, purple). Finally, a skeleton is constructed (4.) representing a 3D-model of each individual microglial cell (right, bar: 10 µm).

D. Maximum intensity projections of analysed confocal images showing microglial cells in perfused or immersion-fixed slices (bar: 50 µm).

E. Top row: individual microglial cells at each time point respective to section C) above (yellow: cell body; blue, purple: processes; bar: 5 µm). Bottom row: reconstructed skeletons for each cell depicted in middle row, together with their sphericity values (black) and total number of process endings (violet, cell body: red dot, bar: 5 µm).

F. Quantification of extracted morphological features regarding sphericity in cortex (green) and in hippocampus (pink). N=8 animal, p.n.: ~35 days; Mann-Whitney, ns: not significant, *: p<0.05, **: p<0.01, ***: p<0.001, ****: p<0.0001.

G. Same as in E) regarding number of process endings / cell in cortex (green) and in hippocampus (pink). N=8 animal, p.n.: ~35 days; Mann-Whitney, ns: not significant, *: p<0.05, **: p<0.01, ***: p<0.001, ****: p<0.0001.

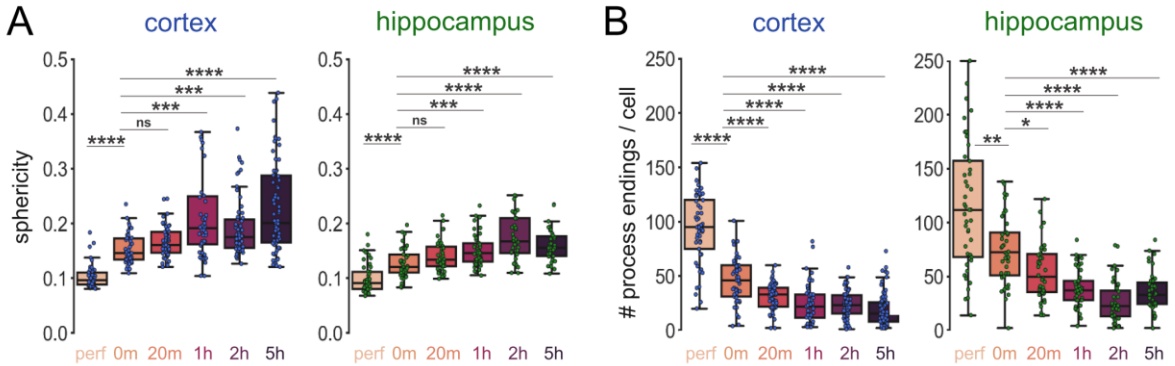

Supplementary Figure 1: Morphological changes of microglia in acute slice preparations obtained from an older group of mice (p.n.: ~95 days)

A. Quantification of extracted morphological features regarding sphericity in cortex (green) and in hippocampus (pink). CX3CR1$^{+/GFP}$ littermates, N=5 animal, p.n.: ~95 days; Mann-Whitney, ns: not significant, *: p<0.05, **: p<0.01, ***: p<0.001, ****: p<0.0001.

B. Same as in E) regarding number of process endings / cell in cortex (green) and in hippocampus (pink). N=5 animal, p.n.: ~95 days; Mann-Whitney, ns: not significant, *: p<0.05, **: p<0.01, ***: p<0.001, ****: p<0.0001.

Rapid downregulation of P2Y12R is accompanied by gradual depolarization during the incubation process

To further investigate the extent of microglia activation during the incubation process, we next examined changes in microglial P2Y12 receptor (P2Y12R) levels, through which microglia sense and influence neuronal activity and fate (Cserép et al., 2020; Dissing-Olesen et al., 2014; Eyo et al., 2014; Gu et al., 2016; Kato et al., 2016), and which are downregulated upon inflammatory challenges (Haynes et al., 2006; Mildner et al., 2017). Standard pre-embedding immunofluorescent labelling indicated a marked reduction of P2Y12R labelling intensity already 1 hour after slice preparation (Figure 3A).

To quantitatively examine these changes during the whole incubation process, acute slice preparations were immersion-fixed at different time points during incubation (Figure 3B), followed by visualization of P2Y12R with a recently developed quantitative post-embedding immunofluorescent labelling technique (Holderith et al., 2020), enabling unbiased assessment of P2Y12R labelling intensity changes (Figure 3C). We quantified P2Y12R labelling intensity at microglial cell bodies (Figure 3D, left), thick processes (Figure 3D, middle) and thin processes (Figure 3D, right), to investigate whether different subcellular compartments are affected to a different extent. Confirming our immunofluorescent results, we found a consistent, rapid decrease in P2Y12R labelling intensity in all of these compartments until 1 hour of incubation, followed by a small increase towards the 5 hour time point (Figure 3E). This course of downregulation and subsequent modest upregulation turned out to be the most prominent in thick and thin processes (Figure 3E, middle, right), while P2Y12R levels at microglial cell bodies seemed to be less affected by the slice preparation procedure (Figure 3E, left). As such, after 1 hour of incubation the labelling intensity (arbitrary unit, see: Methods) dropped by 25% on thick processes ($p<0.01$), 29% on thin processes ($p<0.001$) and 20% at cell bodies.

Microglial phenotype changes have also been shown to correlate with changes in resting membrane potential, while the tonically active K+ channels responsible for maintaining resting membrane potential are known to be potentiated by P21Y12R actions (Madry, Kyrargyri, et al., 2018; Swiatkowski et al., 2016), especially in response to injury when high ATP/ADP exposure occurs. Therefore, rapid P21Y12R downregulation is expected to be accompanied with membrane depolarization. To test this, we performed electrophysiological recordings from microglia in acute slices. As in previous experiments, acute slice preparations were placed into an interface type incubation chamber for recovery and then transferred to a recording chamber at different time points during incubation, to measure microglia in whole cell patch-clamp configuration. Targeting of microglial cells was guided by the intrinsic GFP signal across the hippocampal CA1-CA3 stratum lacunosum-moleculare and stratum radiatum regions, and below ~40 µm measured from the slice surface (Figure 3F). Our results showed that microglial cells became gradually more depolarized throughout the total 5 hours of the incubation process (Figure 3G, left; N=158 cells measured in slices from a total of 10 animals), while we did not observed significant changes in input resistance (Figure 3G, right). Taken together, microglia undergo rapid phenotype changes in acute slice preparations, as characterized by cell body and process translocation (Figure 1), quick morphological shift towards an "amoeboid" shape (Figure 2), as well as early P2Y12R downregulation and gradually depolarizing resting membrane potential (Figure 3).

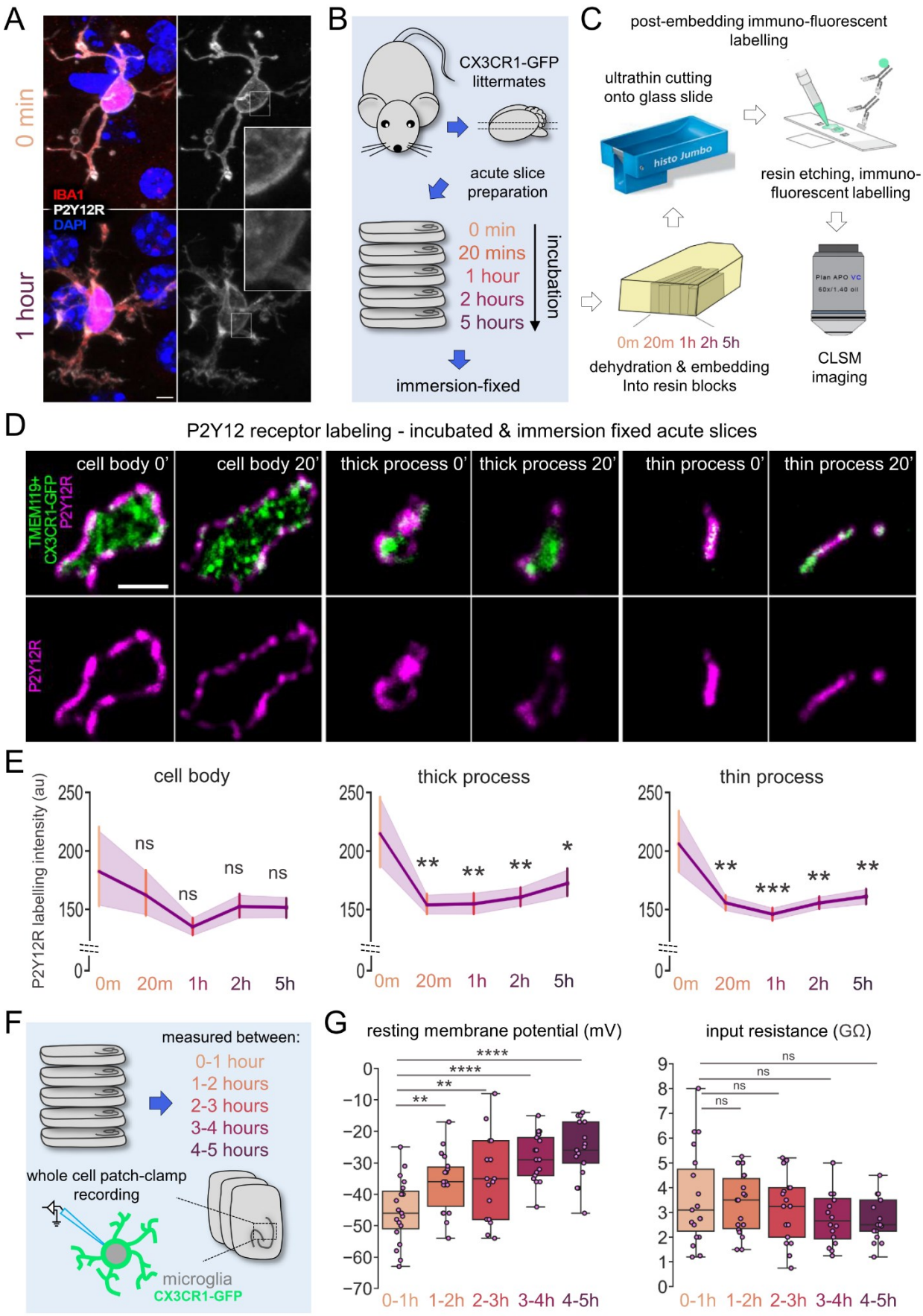

Figure 3. Rapid downregulation of P2Y12R is accompanied by gradual depolarization during the incubation process

A. Single image planes of multi-channel confocal laser scanning microscopy z-stacks, depicting microglial cells with pre-embedding immunofluorescent labelling (IBA1, red; P2Y12 receptors, white) before (0 min) and after 1 hour of incubation (bar: 3 µm).

B. Schematic representation of the experiment. CX3CR1$^{+/GFP}$ littermates (N=3; p.n.: ~35 days) were used to create acute hippocampal slice preparations and placed into an interface-type incubation chamber for recovery. Slices were immersion-fixed before (0 minute) or after 20 minutes, 1 hour, 2 hours and 5 hours of incubation.

C. After fixation, P2Y12 receptor labelling was performed by a post-embedding immunofluorescent labelling technique: slices were dehydrated and embedded into resin blocks. Subsequently, ultrathin slices were cut onto glass slides and labelled after resin etching. Finally, z-stack images were gathered from preparations via high-resolution confocal laser scanning microscopy.

D. Representative images of P2Y12 receptor labelling via the post-embedding technique. Microglial cell bodies (left), thick processes (middle) and thin processes (right) are shown together with the P2Y12R labelling (top row) and P2Y12R labelling only (bottom row) at 0 and 20 minute time points (bar: 2 µm).

E. Quantification of P2Y12 receptor labelling intensity (arbitrary unit, see: Methods) in microglial cell body (left), thick processes (middle) and thin processes (right.) N=3 animal, p.n.: 35 days; 3 slices/animal; independent t-test, ns: not significant, *: p<0.05, **: p<0.01, ***: p<0.001.

F. Schematic representation of the experiment. CX3CR1$^{+/GFP}$ littermates (N=10, p.n.: ~95 days) were used to create acute slices. Microglial cells were measured in whole cell patch-clamp configuration. Microglial cells were targeted via their intrinsic GFP signal across the hippocampal CA1-CA3 stratum lacunosum-moleculare and stratum radiatum regions.

G. Resting membrane potential (left) and input resistance (right) of individual microglial cells at different time points of the recovery process. N=10 animal, p.n.: ~90 days; N=158 cells measured in total; independent t-test, ns: not significant, *: p<0.05, **: p<0.01, ***: p<0.001.

Microglial phenotype changes are accompanied by rapid alterations of microglia-neuron interactions

Next, we wanted to investigate whether changes in microglial phenotype paralleled altered microglia-neuron interactions in acute slice preparations. To this end, we looked at microglial contacts with synaptic elements and neuronal cell bodies (Cserép et al., 2020), in order to examine how the number of these contacts might change during the incubation process. Native GFP-signal of microglia was enhanced by anti-GFP labelling, neuronal cell body identification was established via Kv2.1 labelling, and synaptic elements were identified via VGLUT1-Homer1 and VGAT-Gephyrin co-localization (Figure 4A, C).

We found that the total percentage of neuronal soma contacted by microglial processes gradually decreased throughout the incubation process and dropped by ~23% (independent t-test, $p<0.01$) after 5 hours of incubation (Figure 4B, left). We also investigated how the percentage of somatic area covered by microglial processes changed over time, which has doubled at 0 minutes compared to the perfused controls (from 4% to 8%, independent t-test, $p<0.05$). This observation indicates extremely rapid microglia actions taking place during the ~1-3 minutes between brain extraction and slice fixation. The massive initial increase was followed by a gradual decrease dropping back again to control values (purple indication; independent t-test, $p<0.05$) after 5 hours of incubation (Figure 4B, right). In line with this, microglia-synapse contact prevalence showed similar alterations after slice preparation in the case of glutamatergic synapses (Figure 4D, left), where average percentage of contacts increased by 46% between the perfused and 0 minute conditions (independent t-test, $p<0.05$) and gradually dropped back to control values. In the case of GABAergic synapses (Figure 4D, right), we did not observe significant increase immediately after slice preparation, however we measured a prominent and gradual decrease in contacts during the incubation process resulting in a 42% drop after 5 hours of incubation (independent t-test, $p<0.0001$). Based on these

observations, we concluded that microglia-neuron interaction sites underwent rapid and progressive changes, as somatic coverage and contact prevalence on glutamatergic synapses significantly increased immediately after slice preparation, followed by a gradual decrease over time.

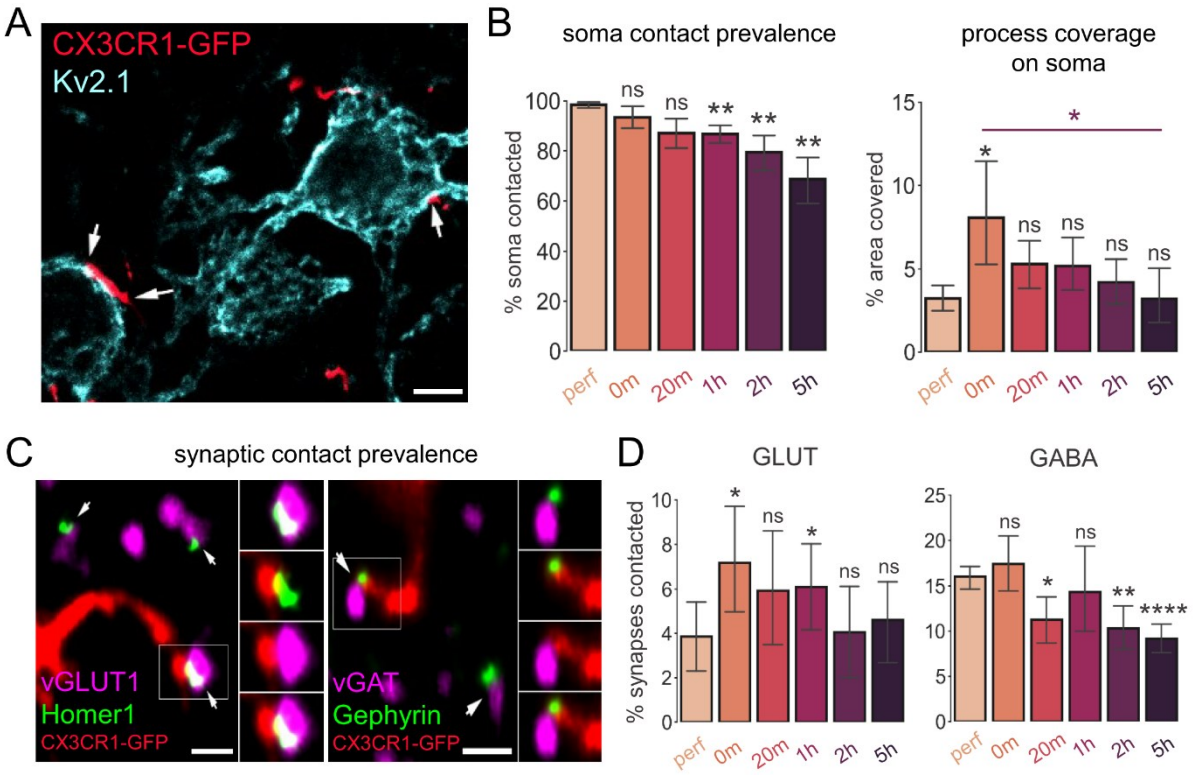

Figure 4. Microglial phenotype changes are accompanied by rapid alterations of microglia-neuron interactions

A. Representative section of a maximum intensity projection image created from confocal z-stacks used to quantify microglial contact prevalence and process coverage on neuronal soma. White arrows point to areas (overlap of microglia and Kv2.1 labelling) where microglial processes are likely to form contacts on neuronal soma (bar: 5 µm).

B. Quantification of contact prevalence (left) and coverage (right) of neuronal soma by microglial processes (left). N=3 animal, p.n.: ~90 days; independent t-test, ns: not significant, *: p<0.05, **: p<0.01. Black statistical indication: perfused values vs. 0 min – 5 hours. Purple statistical indication: 0 min vs. 5 hours.

C. Single image planes from confocal z-stacks used to quantify contact prevalence of microglial processes onto glutamatergic (left) or GABAergic (right) synapses. (Inserts show image channel pairs from the boxed area, from top to bottom: pre- and postsynaptic marker, microglia and postsynaptic marker, microglia and presynaptic marker, merged.) Arrows show identified individual synapses contacted by microglial processes (bars: 1 µm).

D. Quantification of microglial contact prevalence onto glutamatergic (left) or GABAergic (right) synapses. N=3 animal, p.n.: ~90 days; independent t-test, ns: not significant, *: p<0.05, **: p<0.01, ****: p<0.0001.

Synaptic sprouting is accompanied by increased Sharp Wave-Ripple activity after acute slice preparation

Given the observed changes in microglial contact prevalence on synapses, we next examined how the density of synaptic elements changed during the incubation process. To this end, we used the quantitative post-embedding labelling method to precisely determine both glutamatergic and GABAergic synaptic density changes (Figure 5A) in acute slices.

We found significant increase in both glutamatergic (20% increase compared to 0 min, independent t-test, $p<0.01$) and GABAergic (9% increase compared to 0 min, $p<0.05$) synaptic densities after 1 hour of incubation (Figure 5B), similarly to that seen in previous studies (Bourne et al., 2007; Kirov et al., 1999; Trivino-Paredes et al., 2019). Interestingly, measuring synapse densities at multiple time points during the incubation process revealed robust time-dependent changes concerning the proportions of excitatory and inhibitory synapses. While we observed similar, gradual increase in glutamatergic and GABAergic synaptic density towards the 1 and 2 hour time points, there seemed to be an interesting 1 hour lag in the case of GABAergic synapses (Figure 5B, left vs. right), which peaked after 2 hours of incubation (20% increase compared to 0 min, independent t-test, $p<0.001$). Coincidentally, we observed a significant drop in glutamatergic synaptic density which occurred between 1 and 2 hours of incubation (Figure 5B left, purple statistical indication; 9% drop, independent t-test, $p<0.05$). We observed the highest density of glutamatergic synapses after 5 hours (28% increase compared to 0 min, independent t-test, $p<0.01$), whereas at this time point there was a tendency of decrease in GABAergic synaptic density (Figure 5B right; pink statistical indication; 10% drop, independent t-test, n.s., $p=0.051$). Based on these observations, we concluded that the neuronal network is most likely to be reorganized by the slow and gradual build-up of excitatory synapse numbers, which is followed by the inhibitory synapses in the same manner.

The inhibitory sprouting seemed to reach its maximum after 2 hours of incubation, while excitatory synapse numbers further increased towards the 5 hour time point.

Since the slice preparation approach has been previously optimized to enable the recording of spontaneously occurring SWR events (Hájos et al., 2009; Schlingloff et al., 2014), we examined whether these synaptic changes are also accompanied by changes in the activity of the hippocampal network. To this end, acute hippocampal slice preparations were transferred at specific time points from the incubation chamber into a dual-perfusion recording chamber (Hájos & Mody, 2009) to measure spontaneously occurring sharp wave-ripple (SWR) activity via local field potential (LFP) recordings (Figure 5C). As a readout for network activity changes, we compared SWR amplitude, rate and Ripple amplitude registered from the CA3 pyramidal cell layer of the hippocampus (Figure 5D, E). Our results showed that there was a significant increase in SWR amplitude (76%, Kruskal-Wallis test, $p<0.01$), rate (55%, $p<0.01$) and Ripple amplitude (91%, $p<0.01$) in slice preparations measured between 1 and 2 hours of incubation (Figure 5F), where after the amplitude of events and Ripple amplitude started to gradually decrease, while SWR rate remained at elevated levels towards the 5 hours' time point. Based on these observations, we concluded that gradual excitatory and inhibitory synaptic density changes show correlations with the quality of neuronal activity in our acute slice preparations, since we observed the highest synaptic densities in parallel with increased amplitude and rate in SWR activity.

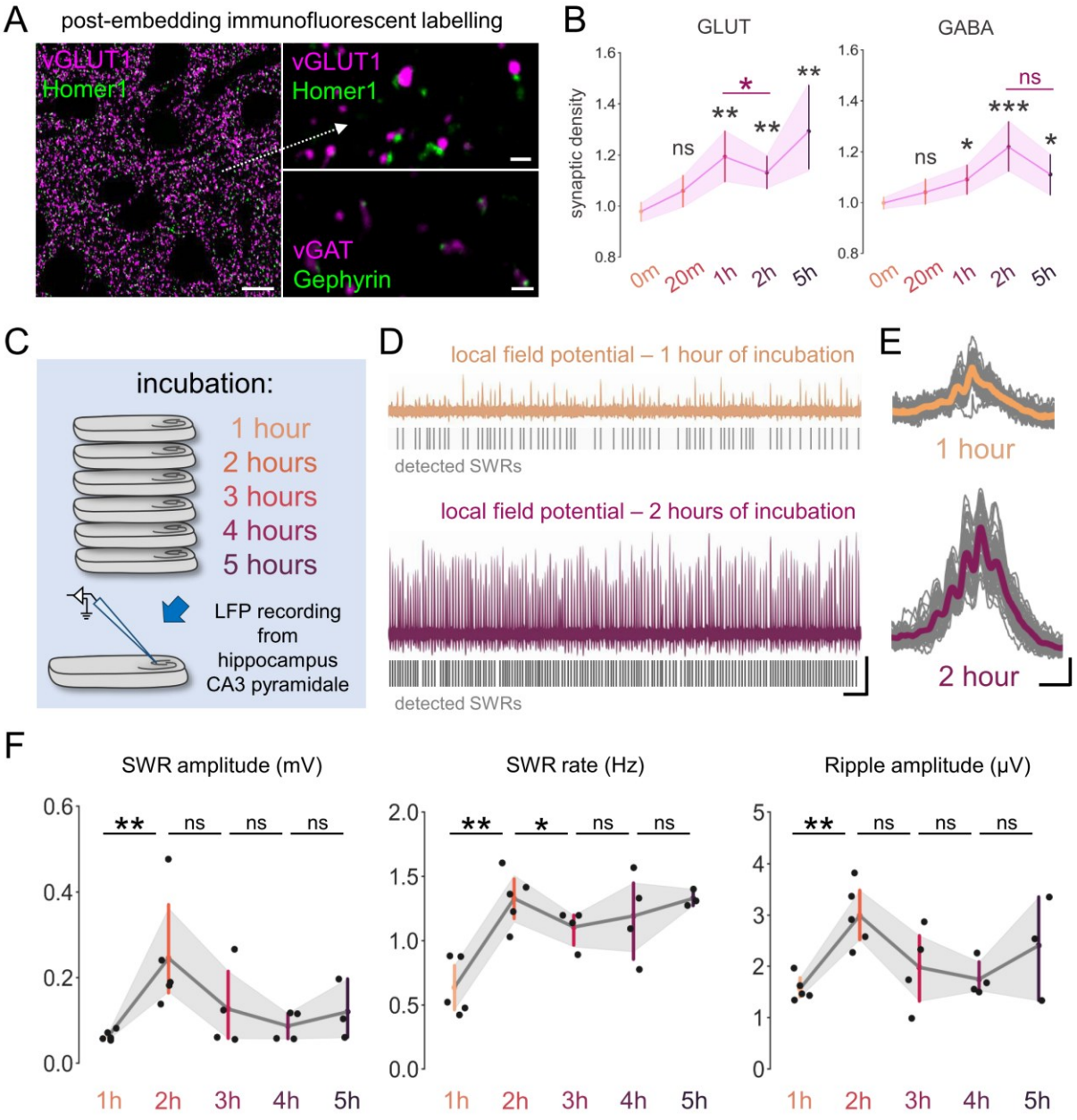

Figure 5. Synaptic sprouting is accompanied by increased Sharp Wave-Ripple activity after acute slice preparation

A. Representative sections of maximum intensity projection images created from confocal z-stacks used to quantify glutamatergic and GABAergic synaptic densities. Images were created using the post-embedding labelling technique. A large area of glutamatergic synaptic labelling is shown (left, bar: 5 µm) and zoomed-in insets of glutamatergic (right, top; bar: 1 µm) and GABAergic synaptic labelling (right, bottom; bar: 1 µm).

B. Quantification of synaptic density changes during the incubation process regarding glutamatergic (left) and GABAergic (right) synapses. N=6 animal, p.n.: ~65 days; independent t-test, ns: not significant, *: p<0.05, **: p<0.01, ***: p<0.001.

C. Schematic representation of the experiment. CX3CR1$^{+/GFP}$ littermates (N=8; p.n.: ~65 days) were used to create acute hippocampal slice preparations and placed into an interface-type incubation chamber for at least 1 hour of recovery time. Subsequently, slices were transferred at specific time points (hourly after 1-5 hours) into a recording chamber to measure sharp-wave ripple (SWR) activity via local field potential recordings (LFP) registered from the CA3 pyramidal layer of the hippocampus.

D. Representative LFP recordings measured after 1 (yellow) or 2 hours (purple) of incubation. Grey lines represent detected SWR events (bars 10 s, 50 µV).

E. Representative averaged traces of detected SWRs (#50 in total) measured after 1 hour (yellow: average, grey: individual events) or 2 hours (purple: average, grey: individual events) of incubation (bars 100 ms, 25 µV).
F. Quantification of SWR amplitude (left), rate (right) and Ripple amplitude (right) comparing events measured after different time spent in the incubation chamber before recording. N=8 animal, p.n.: 65 days; Kruskal-Wallis test, ns: not significant, *: p<0.05, **: p<0.01.

The absence of microglia disrupts time-dependent synaptic sprouting in acute slices

Increasing evidence suggests that microglial cells are essential for the formation, pruning and maintenance of synapses both in the developing and in the adult CNS (Ikegami et al., 2019). We wanted to examine whether microglia can also actively contribute to the observed time-dependent structural and functional changes in synaptic density detected in acute slice preparations. To this end, we measured changes of synaptic densities in acute slice preparations in the absence of microglia (induced by elimination of microglia with PLX5622 for three weeks *in vivo* prior to slice preparation, Figure 6A-B). Depletion of microglia with PLX3373 or PLX5622 *in vivo* has previously been shown to induce no substantial changes in neuronal cell numbers and morphology, as well as they caused no deficits in cognition and behaviour, although dendritic spine numbers showed a slight increase (Elmore et al., 2014; Han et al., 2017; Strackeljan et al., 2021). To measure and compare synaptic density changes between control (CTRL) and depleted (DEPL) condition, we used the previously described post-embedding labelling method (Figure 6C).

We found that time-dependent synaptic density changes after slice preparation were markedly influenced by microglial actions (Figure 6D). To our surprise, the absence of microglia abolished the gradual increase of glutamatergic synaptic density observed under control conditions, and – after a slight and non-significant increase at 1 hour – returned to the initial values after 5 hours, resulting in a 27% lower synaptic density in DEPL compared to CTRL, ($p<0.001$, Figure 6D, left).

Even more prominent differences were observed regarding GABAergic synaptic densities (Figure 6D, right). The absence of microglia led to a marked initial increase of GABAergic synaptic density, peaking at 1 hour, followed by a radical drop at 2 hours and a slight increase after 5 hours. This course fundamentally differs from the delayed and gradual increase observed under control conditions, which peaks at 2 hours (19% higher in CTRL, $p<0.001$, Figure 6D, right). These results clearly indicate that microglia differentially controls excitatory and inhibitory synaptic sprouting in acute slice preparations, initiating glutamatergic, while repressing GABAergic synapse formation, at least during the early stages (<1hour) following acute slicing.

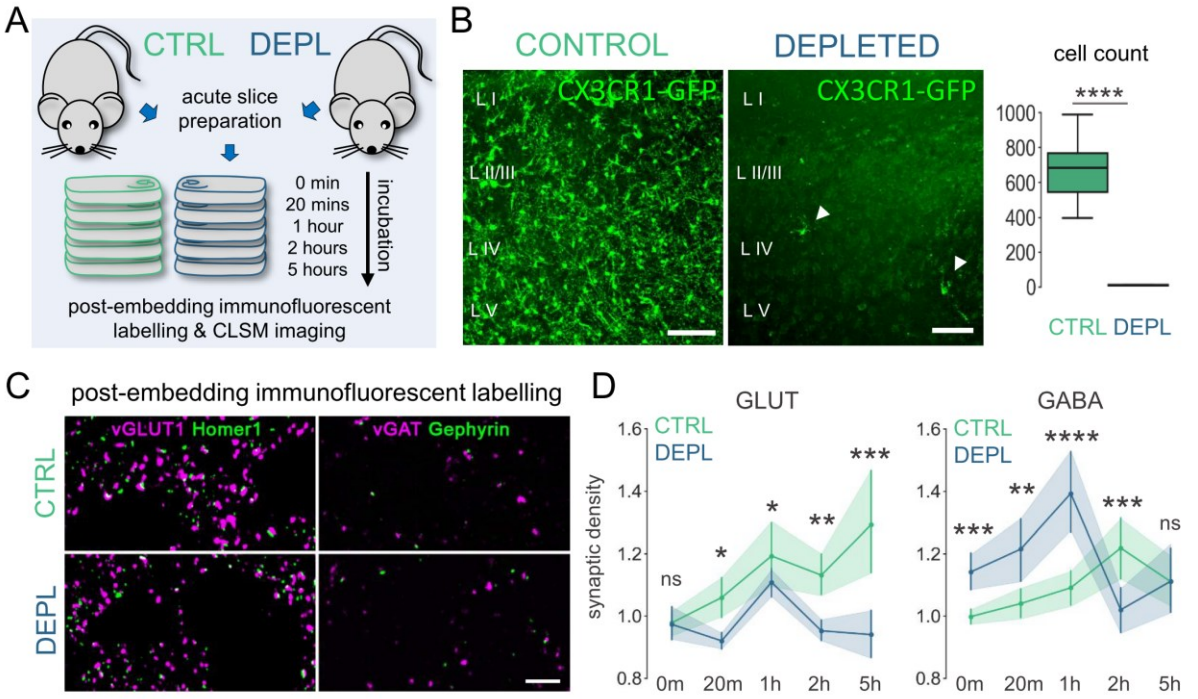

Figure 6. The absence of microglia disrupts time-dependent synaptic sprouting in acute slices

A. Schematic representation of experiment. CX3CR1$^{+/GFP}$ littermates were used to create a control (CTRL; N=3, p.n.: ~65; green) and a microglia depleted (DEPL; N=3, p.n.: ~65; blue) subgroup of animals. Slice preparations were obtained from both groups and immersion-fixed at different time points during recovery.

B. Maximum intensity projection images showing microglial cells in acute slice preparations obtained from animals that either belong to control (left) or depleted (middle) group (bars: 100 µm). Quantification comparing the total number of microglial cells counted in control (CTRL, blue) or depleted (DEPL, green) acute slices (right). N=6-6 animal, p.n.: ~65 days; independent t-test, ns: not significant, ****: $p<0.0001$.

C. Representative sections of maximum intensity projection images created from confocal z-stacks used to quantify and compare densities of glutamatergic (left) or GABAergic (right) synapses in control (top row) or microglia depleted (bottom row) acute slices (bar: 5 µm).

D. Quantification of synaptic density changes during the incubation process regarding glutamatergic (left) and GABAergic (right) synapses. Synaptic density changes are compared between control (green, data also shown in Figure 5b) and microglia depleted (blue) acute slices. N=6 animal, p.n.: 65 days; independent t-test, ns: not significant, *: p<0.05, **: p<0.01, ***: p<0.001, ****: p<0.0001.

The absence of microglia impairs Sharp Wave-Ripple activity in acute slice preparations

We observed markedly lower glutamatergic and GABAergic synaptic densities after 2 hours of incubation when microglia were absent (Figure 6D), while in parallel SWR parameters showed a significant increase in control slices after 2 hours (Figure 5F). Thus, we set out to examine whether synchronous events are also positively affected by the presence of microglia. To this end, we decided to compare features of spontaneously occurring SWR activity measured from control (CTRL) or microglia depleted (DEPL) acute slice preparations using simultaneous recordings from both conditions (Figure 7A-B).

Since we measured slice preparations from both groups at the same time and for the same duration, we decided to quantify and compare the differences concerning the occurrence of SWR activity between the two conditions. We observed that 18 out of 36 slices (50%) presented detectable SWR activity in CTRL (for more detail in evaluation, see: Methods), whereas only 4 out of 36 slices (11%) from DEPL (Figure 7C). Furthermore, our results showed significant differences between spontaneously occurring SWR activity recorded from CTRL or DEPL acute slice preparations, as we observed ~3.5 fold decrease in SWR amplitude, ~1.9 fold decrease in SWR rate and ~2.1 fold decrease in Ripple amplitude registered from DEPL when compared to CTRL slices (Figure 7D). Quantification showed a median value of SWR amplitude (in mV) 0.109 (q1: 0.058, q3: 0.191) in the case of CTRL and 0.032 (q1:0.021, q3: 0.04) in the case of DEPL conditions (Mann-Whitney test, $p<0.001$). Concerning SWR rate, we measured (in Hz) 1.21 (q1: 0.86, q3: 1.37) in CTRL condition, and 0.62 (q1: 0.47, q3: 0.88) in case of DEPL condition ($p<0.05$). We measured the Ripple amplitude to be (in μV) 2.27

(q1: 1.59, q3: 2.86) in the case of CTRL and 1.07 (q1:0.82, q3: 1.23) in the case of DEPL conditions ($p<0.01$). These results indicate that microglia can effectively support the neuronal network in slice preparations during the incubation process, and can positively influence the occurrence, amplitude and frequency of spontaneously occurring SWR activity.

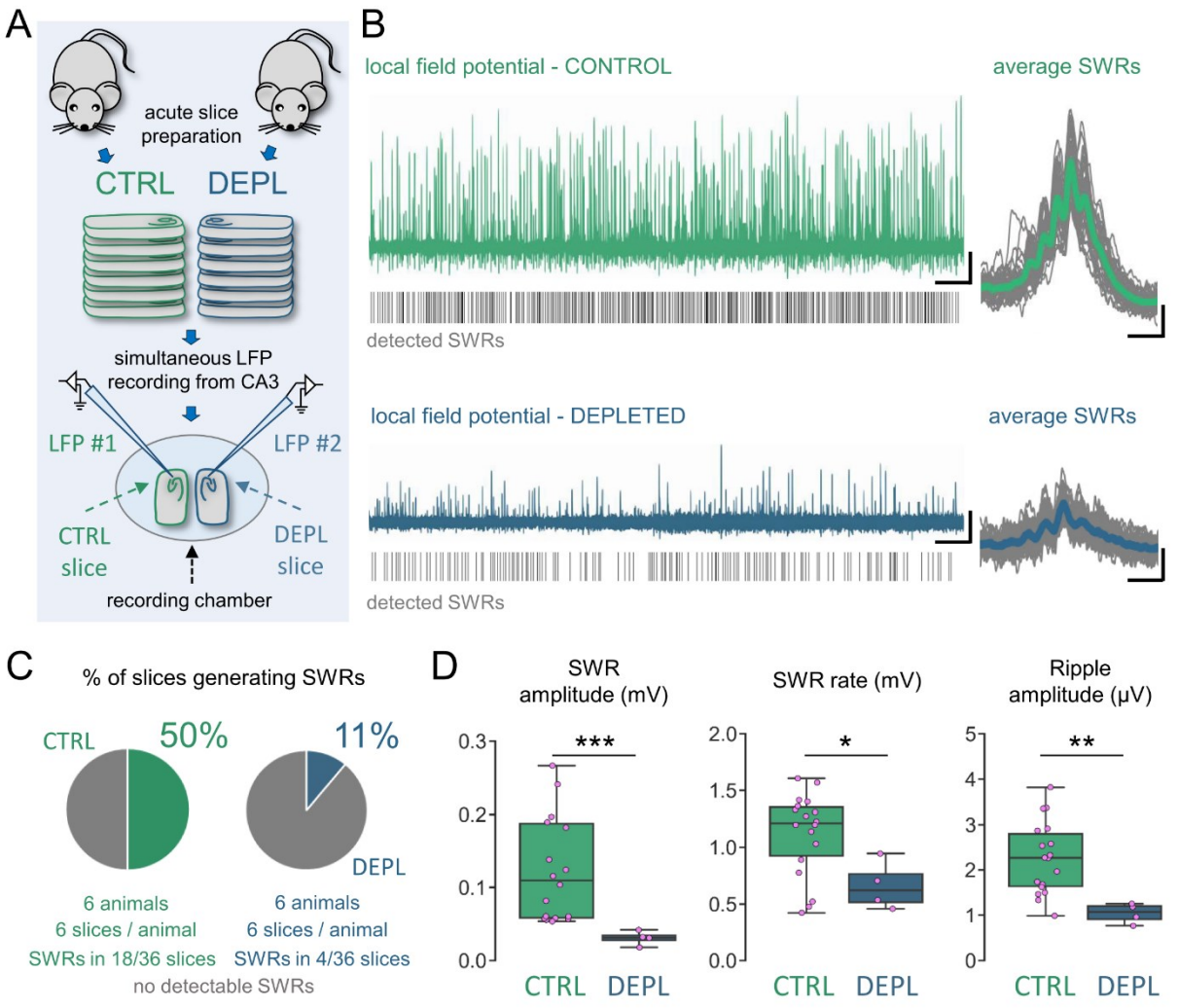

Figure 7. The absence of microglia impairs Sharp Wave-Ripple activity in acute slice preparations

A. Schematic representation of experiment. CX3CR1$^{+/GFP}$ littermates were subjected to 3 weeks of either control or PLX3397 containing diet to create a control (CTRL; N=6, p.n.: ~65; green) and a microglia depleted (DEPL; N=6, p.n.: ~65; blue) subgroup of animals. Acute hippocampal slice preparations were obtained from both groups and placed into an interface-type incubation chamber for at least 1 hour of recovery. Subsequently, slices were transferred together in a pairwise manner into a recording chamber, to simultaneously measure sharp wave-ripple (SWR) activity via local field potential recordings (LFP) registered from the CA3 pyramidal layer of the hippocampus.

B. Representative LFP recordings (left; bar: 30 s, 50 µV) and averages of spontaneous SWR events (right; #50 in total, bar: 100 ms, 25 µV) registered from control (top row, green) and microglia depleted (bottom row, blue) slices. Grey lines represent detected SWR events.

C. Pie-charts representing SWR activity occurrence in measured slices from control group (green, 18/ 36 slices) versus microglia depleted (blue, 4/36 slices).

D. Quantification of SWR amplitude (left), rate (middle) and Ripple amplitude (right) comparing events measured from control (CTRL, green) or depleted slices (DEPL, blue). N=6 animal/group, p.n.: ~65 days; Mann-Whitney test, ns: not significant, *: p<0.05, **: p<0.01, ***: p<0.001.

Discussion

In this study, we investigated how microglial cells react to the acute slice preparation and incubation procedure, while we simultaneously examined how key sites of microglia-neuron interactions and the spontaneous activity of the neuronal network is affected. We show that the microglial cell population undergoes rapid, robust and progressive phenotype changes towards a reactive state in acute slice preparations. This behaviour is reflected in rapid downregulation of P2Y12 receptors located on thick and thin processes, a gradual depolarization of resting membrane potential, translocation of cells towards the slice surfaces and a reduced process density in the neuropil due to transitioning into an "amoeboid" morphology. Furthermore, our results confirm that interactions between microglial processes and neuronal somata or synapses undergo significant changes immediately after slice preparation. In line with this, our results indicate that microglia heavily influence synaptic sprouting in acute slices and can actively support the neuronal network to produce spontaneously emerging SWR activity.

We first aimed to study how the slice preparation procedure affected microglial cells in acute slices. Locomotive and process polarization behaviour of microglia has been observed previously in slice preparations, which was ultimately directed towards dead or injured cells in the vicinity of microglia (Petersen & Dailey, 2004; Stence et al., 2001). However, population level changes in the distribution of cell bodies and processes along the full depth of slices were not investigated in a time-dependent manner before. Microglial recruitment to the site of injury is known to be driven by extracellular ADP and P2Y12R actions (Davalos et al., 2005; Haynes et al., 2006; Nasu-Tada et al., 2005), which in the case of acute slices is more likely to realize near the surface of preparations, where the highest concentration of dead cells and cellular

492 debris is expected. To our knowledge, we show for the first time that microglial cell bodies
493 gradually migrate and extend their processes towards the surface of slices. Interestingly, we
494 also show that microglia translocation towards the slice surfaces is asymmetric, as it is more
495 prominent towards the top surface (facing towards the upper surface of the interface chamber).
496 It is possible that a gradually decreasing level of oxygenation along the depth of the slice, as
497 well as a higher neuronal activity at the top surface could be a driving factor beside the injury-
498 related signals (Huchzermeyer et al., 2013; Ivanov & Zilberter, 2011; Mulkey et al., 2001). It
499 is important to note here that a general rule in electrophysiological investigations of microglia
500 is to avoid measurements taking place at the top 30-50 µm of slice preparations (Avignone et
501 al., 2019). Our results confirm that this region is indeed the most susceptible for rapid changes
502 in microglial phenotypes, as we saw highest changes in microglial cell body and process
503 densities in the top layer, whereas layers towards the bottom of slices seem to be less affected.
504 However, our results also indicate that experimenters should expect an increased density of
505 reactive microglia over time even in the lowest regions of the slice, and measuring deep in the
506 tissue in itself cannot prevent findings from being influenced by the emergence of more
507 reactive microglial phenotypes over time.

508 Injury or tissue disturbance has been shown to extensively stimulate and recruit
509 microglia resulting in drastic morphological changes during reactive microgliosis (Kettenmann
510 et al., 2011; Koshinaga et al., 2000; Savage et al., 2019). Importantly, the acute slice
511 preparation technique can ultimately be considered as a traumatic event resulting in pathologic
512 signals for microglial cells, since rapid transitioning to an amoeboid phenotype has been
513 observed before in acute slices prepared via different methodologies (Kettenmann et al., 2011;
514 Matyash et al., 2017; Petersen & Dailey, 2004; Stence et al., 2001). In line with previous
515 studies, we show that robust morphological changes are already present immediately after slice
516 preparation when compared to perfusion fixed tissue, and changes during the incubation seem

517 to generally consolidate after 1 hour, when cells reach a more "amoeboid" phenotype. It is
518 important to note that the extent of these changes are indicative of severe pathological
519 conditions, since morphological characteristics of microglia after 1 hour of slice preparation
520 are similar to cells measured at peri-infarct cortical areas in experimental stroke models of mice
521 (Morrison & Filosa, 2013; Sadler et al., 2020; Singh et al., 2018) and in severe Alzheimer's
522 disease patients (Davies et al., 2017).

523 The extensive expression of P2Y12 receptors (P2Y12R) are widely considered to be a
524 signature of microglia in the healthy brain (Bosco et al., 2018; Hickman et al., 2013; Peng et
525 al., 2019), while downregulation of P2Y12R is generally observed in pathologies and
526 associated with a reactive phenotype (Lin et al., 2021; Tóth et al., 2022; Zrzavy et al., 2017).
527 Drastic downregulation of P2Y12Rs were observed in slice cultures as well, but changes were
528 monitored in a longer timeframe (0, 8, 24 hours), and the extent has been shown to correlate
529 strongly with microglia morphology (Haynes et al., 2006). Our observations are in line with
530 these results, while we show with a fully quantitative post-embedding method (Holderith et al.,
531 2020) that rapid downregulation of P2Y12R occurs most extensively at the processes of
532 microglia already after 1 hour of incubation. Interestingly, we show that P2Y12R
533 downregulation seem to consolidate after 1 hours of incubation, similarly to the observed
534 changes in morphology. This observation further strengthens the functional correlation
535 between changes in P2Y12R expression and the transformation into a reactive phenotype. In
536 addition, resting membrane potential of microglia has also been shown to correlate with
537 morphology, as modified activity of tonically active K+ channels responsible for maintaining
538 resting membrane potential (knocking out THIK-1 or locally increasing extracellular [K+]) can
539 decrease ramification (Madry, Arancibia-Cárcamo, et al., 2018; Madry, Kyrargyri, et al.,
540 2018). It has been proposed that transitioning into a reactive phenotype could partly reflect
541 decreased expression of THIK-1 (Madry, Kyrargyri, et al., 2018), as activation via LPS

542 treatment resulted in a significantly downregulated expression of THIK-1 mRNA (Holtman et
543 al., 2015). Importantly, our results indicate that gradual depolarization, rapid P2Y12R
544 downregulation and transitioning into an amoeboid morphology are co-occurring events in
545 acute slice preparations solely at "baseline" conditions, without any additional stimuli present
546 such as LPS or extracellular ATP/ADP.

547 The described changes in P2Y12Rs are highly important when considering microglial
548 and neuronal cell interactions, since P2Y12R function is a key modulator between the two
549 cellular populations (Cserép et al., 2020; Lin et al., 2021; Sipe et al., 2016). We examined the
550 main sites of these interactions, which are thought to be realized between microglial processes
551 and neuronal somata or synaptic elements (Cserép et al., 2020; Miyamoto et al., 2013). We
552 show that while prevalence of contacts on neuronal soma (somatic junctions) slowly and
553 gradually decreases, the percentage of somatic area covered by microglial processes undergoes
554 a more than two-fold increase immediately after slice preparation. This is a key observation,
555 since similar changes in neuronal somatic coverage has been detected in experimental stroke
556 models (Cserép et al., 2020). Furthermore, these changes were co-occurring with a similarly
557 increased and sustained number of contacts on glutamatergic synapses, while contacts on
558 GABAergic synapses were gradually decreasing over the examined timeframe. Based on these
559 observations, our results strongly indicate that microglia behaviour shows similarities to *in vivo*
560 experimental stroke conditions immediately after slice preparation, which action is mainly
561 realized at microglia-neuron somatic junctions (Cserép et al., 2020) and at glutamatergic
562 synapses. Moreover, these results also demonstrate that microglial cells can rapidly redistribute
563 their processes upon pathological stimuli and target specific types of synaptic elements.

564 Studies have previously demonstrated that acute slice preparation induces synaptic
565 sprouting (Bourne et al., 2007; Kirov et al., 1999; Trivino-Paredes et al., 2019), and have
566 consistently shown an excessive proliferation of dendritic spines and increased density of

567 synapses after 1 hour of incubation, when using ice-cold (<4ºC) cutting solution and
568 subsequent warm (35-37ºC) ACSF during recovery (Eguchi et al., 2020). It has also been
569 demonstrated that hippocampal field excitatory postsynaptic potentials (fEPSPs) recover in
570 correlation with these changes (Kirov et al., 1999). Our results are in line with these findings,
571 while we demonstrate that synaptic densities can vary in a time dependent manner during the
572 incubation process, and SWR activity shows a huge increase in amplitude, rate and frequency
573 when both glutamatergic and GABAergic synaptic densities are sufficiently increased (after 2
574 hours of incubation). Since the generation of SWRs in these conditions are both reliant on a
575 sufficiently large tonic excitatory activity and the action of reciprocally connected parvalbumin
576 positive basket cells (Schlingloff et al., 2014), these results indicate that a delicate balance
577 needs to be maintained between excitation and inhibition during the course of sprouting which
578 allows SWRs to emerge. In this study, we show that microglia has a major effect on how these
579 synaptic density changes are realized in acute slice preparations, as absence of microglia
580 changes the course of synaptic sprouting drastically. Importantly, microglial contacts can
581 facilitate spine formation and the development of functional synapses, which function is
582 correlated to an activated phenotype of microglia during early development (Miyamoto et al.,
583 2016). Furthermore, partial depletion of microglia can cause more asynchronous activity
584 without overall change in frequency (Akiyoshi et al., 2018), and similar depletion in the
585 hippocampus resulted in decreased spontaneous and evoked glutamatergic activity and
586 decreased glutamatergic synaptic density (Basilico et al., 2022). In contrast, *in vivo* imaging
587 experiments showed a rather increased excitatory and inhibitory neuron activity in the cortex
588 after microglia depletion, which results were consistent with *ex vivo* circuit mapping data (Liu
589 et al., 2021, 2022). In line with these studies, our results indicate that microglia can facilitate
590 glutamatergic and represses GABAergic synaptic formation in order to maintain a balanced
591 reorganization of the network after the loss of synapses due to the slice preparation procedure.

We also show that this microglia modulated synaptic reorganization can happen within hours after injury, therefore this effect should be taken into consideration in other specific *in vivo* or *ex vivo* investigations of injury related behaviour of microglia and the neuronal population, particularly in models for stroke, ischemia and brain trauma. Examination of the microglial contribution to these short-term synaptic changes could help us better understand underlying mechanisms behind these pathologies.

To our knowledge, we show for the first time that the presence of microglia can actively influence SWR activity in hippocampal acute slice preparations. Taken together, we show that microglial cells are active players in acute slice preparations and can heavily influence the activity of the neuronal network.

The acute slice preparation is a well-established experimental tool, which is extremely useful to study the physiology of neurons and other cells from individual synapses to complex neuronal networks. However, precautions are necessary during the interpretation of results, what type of physiological (or pathological) states certain changes in these conditions may reflect concerning both neurons and microglia themselves. In fact, we show that microglial cells in acute slices can present a rapid transition into a more reactive phenotype and can actively influence the neuronal network through interactions via synaptic structures and neuronal somata. Since microglial morphology strongly reflects the state of the tissue, we suggest that monitoring these changes should always be considered, as it could help in the contextualization of results concerning both the microglial and neuronal populations. Moreover, an extensive examination and comparison of microglial phenotype state changes due to different slice preparation methods could facilitate more refined and consistent experimental models and paradigms to be established. In addition, our results also emphasize the importance of interactions between microglia and complex neuronal networks, which may be further emphasized by the sensitivity of microglia to a broad range changes in their micro-

and macroenvironment. While the observed changes in microglia in acute slices may not represent an undisturbed physiological state, the acute slice model also emerges as an instrumental tool to test and understand the different factors, which contribute to reactive microglial phenotypes, with broad implications for diseases of the CNS which are influenced by alterations of microglial function.

Materials & Methods

Animals

In all experiments, CX3CR1$^{+/GFP}$ or C57Bl/6J mice littermates of both sexes were used. Mice were kept in the vivarium on a 12 hour light/dark cycle and provided with food and water ad libitum. The animals were housed two or three per cage. All experiments were approved by the Ethical Committee for Animal Research at the Institute of Experimental Medicine, Hungarian Academy of Sciences, and conformed to Hungarian (1998/XXVIII Law on Animal Welfare) and European Communities Council Directive recommendations for the care and use of laboratory animals (2010/63/EU) (license number PE/EA/2552-6/2016; PE/EA/254-7/2019).

Slice preparation, incubation and fixation

In order to minimize bacterial contamination, all the tools and containers used for slice preparation and incubation were routinely cleaned before and after experiments with 70% ethanol and were rinsed extensively with distilled water. For acute slice preparation, mice were decapitated under deep isoflurane anesthesia. The brain was removed and placed into an ice-cold cutting solution, which had been bubbled with *95% O2–5% CO2* (carbogen gas) for at least 30 min before use. The cutting solution contained the following (in mM): *205 sucrose, 2.5 KCl, 26 NaHCO3, 0.5 CaCl2, 5 MgCl2, 1.25 NaH2PO4, 10 glucose*, saturated with *95% O2–5% CO2*. Horizontal hippocampal slices of 300 µm or 450 µm (in case of LFP recordings) thickness were cut using a Vibratome (Leica VT1000S). The process of slice preparation from termination till the first slice to be immersion-fixed took ~2-3 minutes.

After acute slice preparation, slices were placed into an interface-type holding chamber for recovery. In an interface-type chamber, slices are laid onto a mesh just slightly submerged

into the artificial cerebrospinal fluid (ACSF), therefore the oxygenation of the tissue is mainly realized by the direct exposure to humidified oxygen-rich air above the slices. This chamber contained standard ACSF at 35°C that gradually cooled down to room temperature. The ACSF solution contained the following (in mM): *126 NaCl, 2.5 KCl, 26 NaHCO3, 2 CaCl2, 2 MgCl2, 1.25 NaH2PO4, 10 glucose*, saturated with *95% O2–5% CO2*. Immediately after slice preparation/given timeframes of incubation/after recordings, slices were immersion-fixed for 1 hour with 4% PFA solution.

For perfusion-fixed slices, mice were anesthetized and transcardially perfused with 0.9% NaCl solution for 1 minute, followed by 4% PFA in 0.1 M phosphate buffer (PB) for 40 minutes, followed by 0.1 M PB for 10 minutes to wash the fixative out. Blocks containing the somatosensory cortex and ventral hippocampus were dissected, and horizontal sections were prepared on a vibratome (VT1200S, Leica, Germany) at 50 µm thickness for immunofluorescent histological and 100 µm thickness for the automated morphological analysis.

Cross section of slice preparations and quantification of translocation

300 µm thick acute slices were immersion fixed immediately after slicing (0 minute) or after 20 minutes, 1 hour, 2 hours or 5 hours spent in an interface-type incubation chamber (Figure 1A). Fixed slices were washed in 0.1M PB, flat embedded in 2% agarose blocks, rotated 90 degrees, and resliced on a vibratome (VT1200S, Leica, Germany) at 50 µm thickness (Figure 1B). The sections were mounted on glass slides, and coverslipped with Aqua-Poly/Mount (Polysciences). Intrinsic ($CX3CR1^{+/GFP}$) immunofluorescence was analyzed using a Nikon Eclipse Ti-E inverted microscope (Nikon Instruments Europe B.V., Amsterdam, The Netherlands), with a CFI Plan Apochromat VC 20X DIC N2 objective (numerical aperture: 075) and an A1R laser confocal system. We used 488 nm excitation laser (CVI Melles Griot), and image stacks (resolution: 0.62 µm/px) were taken with NIS-Elements AR. Maximal intensity projections of stacks containing the whole section thickness were saved in tiff format, cell bodies were masked with Fiji "Analyze particles" plugin. Cell-body masks were used to count cells, and these masks were subtracted from the original tiff files to get images containing microglial processes only. As a validation for volume-related quantifications in acute slices, the average thickness for each preparation across the incubation procedure was measured (mean±SD: 262±7 µm), which showed no substantial differences between groups (Kruskal-Wallis test, $p>0.05$). For quantification, a measuring grid was placed onto the entire thickness

of cross-sections (Figure 1 C), which divided the thickness into 7 equal zones. Cell body numbers were counted within these grids, and microglial process volume was assessed by measuring fluorescent integrated density within the grids with Fiji software. Cell-body translocation calculation (Figure 1F) was performed for assessing microglial movement towards the top surface, and also for away from the middle Z-depth of the slices. The coordinates for cell bodies were registered in Fiji software, the distance of the cell bodies from the bottom surface or the (middle Z-depth) were measured at 0 min, and also at 5 hours (the number of measured cells was identical at the two time-points). The distances were sorted in growing rows for both time points, and the 0 minute values subtracted from the 5 hour values, thus we could calculate the minimal values cells had to travel in order to reach the final distribution pattern (at 5 hours) starting from the 0 minutes distribution. For the process area coverage measurement (Figure 1I) the images with cell bodies masked out were used. Images from slices fixed at 0 minutes and 5 hours were binarized in Fiji, and the percentage of covered area measured.

Time-lapse imaging

Acute brain slices (300µm thick) were prepared from 80 day old CX3CR1$^{+/GFP}$ mice as described above. Z-stack images (1µm step size) were acquired using a Nikon C2 laser scanning confocal microscope equipped with a 20x CFI Plan Apo VC (NA=0.75 WD=1.00mm FOV=1290.4mm) objective at 488nm, under continuous perfusion with ACSF (3 ml/min perfusion rate). The image acquisition started 1h after slice cutting. Image stacks were taken in every 20min for 6 hours. Video editing was performed using NIS Elements 5.00 and ImageJ 1.53f51.

Automated morphological analysis of microglial cells

300 µm thick acute slices were immersion fixed for 1 hour immediately after slicing (0 minute) or after 20 minutes, 1 hour, 2 hours or 5 hours spent in an interface-type incubation chamber (Figure 1A). Fixed slices were washed in 0.1M PB, flat embedded in 2% agarose blocks, and re-sectioned on a vibratome (VT1200S, Leica, Germany) at 100 µm thickness (Figure 1B). Sections selected from the middle region of incubated slices were immunostained with antibodies, and DAPI (for primary and secondary antibodies used in this study, please see Table 1.). Preparations were kept in free-floating state until imaging to minimize deformation of tissue due to the mounting process. Imaging was carried out in 0.1M PB, using a Nikon

Eclipse Ti-E inverted microscope (Nikon Instruments Europe B.V., Amsterdam, The Netherlands), with a CFI Plan Apochromat VC 60X water immersion objective (numerical aperture: 1.2) and an A1R laser confocal system. Volumes were recorded with 0.2 µm/pixel resolution and a Z-step of 0.4µm. For 3-dimensional morphological analysis of microglial cells, the open-source MATLAB-based Microglia Morphology Quantification Tool was used (available at https://github.com/isdneuroimaging/mmqt). This method uses microglia and cell nuclei labeling to identify microglial cells. Briefly, 59 possible parameters describing microglial morphology are determined through the following automated steps: identification of microglia (nucleus, soma, branches) and background, creation of 3D skeletons, watershed segmentation and segregation of individual cells (Heindl et al., 2018).

Pre-embedding immunofluorescent labelling and analysis of CLSM data

Before the immunofluorescent labelling, the 50 µm thick sections were washed in PB and Tris-buffered saline (TBS). Thorough washing was followed by blocking for 1 hour in 1% human serum albumin (HSA; Sigma-Aldrich) and 0.03-0.1% Triton X-100 dissolved in TBS. After this, sections were incubated in mixtures of primary antibodies, diluted in TBS overnight at room temperature. After incubation, sections were washed in TBS and were incubated overnight at 4 °C in the mixture of secondary antibodies, all diluted in TBS. Secondary antibody incubation was followed by washes in TBS, PB, the sections were mounted on glass slides, and coverslipped with Aqua-Poly/Mount (Polysciences). Immunofluorescence was analyzed using a Nikon Eclipse Ti-E inverted microscope (Nikon Instruments Europe B.V., Amsterdam, The Netherlands), with a CFI Plan Apochromat VC 60X oil immersion objective (numerical aperture: 1.4) and an A1R laser confocal system. We used 405, 488, 561 and 647 nm lasers (CVI Melles Griot), and scanning was done in line serial mode, pixel size was 50x50 nm. Image stacks were taken with NIS-Elements AR. For primary and secondary antibodies used in this study, please see Table 1. Quantitative analysis of each dataset was performed by at least two observers, who were blinded to the origin of the samples, the experiments, and did not know of each other's results.

For the analysis of somatic contact prevalence, confocal stacks with double immunofluorescent labeling (cell type-marker and microglia) were acquired from at least three different regions of mouse cortex. All labeled and identified cells were counted, when the whole cell body was located within the Z-stack. Given somata were considered to be contacted

by microglia, when a microglial process clearly touched it (i.e. there was no space between neuronal soma and microglial process) on at least 0.5 µm long segment.

Microglial process coverage was measured on CLSM Z-stacks acquired with a step size of 300 nm. On single-channel images, Kv2.1-positive cells were selected randomly, the cell bodies of which were fully included in the captured volume. The surface of these cells was calculated by measuring the circumference of the soma on every section multiplied by section thickness. The surface of microglial process contacts was measured likewise.

For the analysis of synaptic contact prevalence, confocal stacks with triple immunofluorescent labeling (pre- and postsynaptic markers and microglia) were analyzed using an unbiased, semi-automatic method. First, the two channels representing the pre- and postsynaptic markers were exported from a single image plane. The threshold for channels were set automatically in FIJI, the „fill in holes" and „erode" binary processes were applied. After automatic particle tracking, synapses were identified where presynaptic puncta touched postsynaptic ones. From these identified points we selected a subset in a systematic random manner. After this, the corresponding synapses were found again in the original Z-stacks. A synapse was considered to be contacted by microglia, when a microglial process was closer than 200 nm (4 pixels on the images).

Post-embedding immunofluorescent labelling and quantitative analysis

The technique described by Holderith et al. (Holderith et al., 2021.) was used with slight modifications. 300 µm thick acute slices were cut from CX3CR1$^{+/GFP}$ mouse line and then immersion fixed immediately after slicing (0 minute) or after 20 minutes, 1 hour, 2 hours or 5 hours spent in an interface-type incubation chamber (Figure 1 B). Fixed slices were washed in 0.1M PB and 0.1M Maleate Buffer (MB, pH: 6.0). Then slices were treated with 1% uranyl-acetate diluted in 0.1M MB for 40 minutes in dark. This was followed by several washes in 0.1M PB, then slices were dehydrated in ascending alcohol series, acetonitrile and finally embedded in Durcupan (Fluca). Each block contained all slices from a respective time series of one animal. Ultrathin sections were cut using a Leica UC7 ultramicrotome at 200 nm thickness, and collected onto Superfrost Ultra plus slides and left on a hotplate at 80°C for 30 minutes then in oven at 80°C overnight (Figure 3 C). Sections were encircled with silicon polymer (Body Double standard kit, Smooth-On, Inc.) to keep incubating solutions on the slides. The resin was etched with saturated Na-ethanolate for 5 minutes at room temperature. Then sections were rinsed three times with absolute ethanol, followed by 70% ethanol and then

DW. Retrieval of the proteins were carried out in 0.02M Tris Base (pH = 9) containing 0.5% sodium dodecyl sulfate (SDS) at 80°C for 80 min. After several washes in TBS containing 0.1% Triton X-100 (TBST, pH = 7.6), sections were blocked in TBST containing 6% BlottoA (Santa Cruz Biotechnology), 10% normal goat serum (NGS, Vector Laboratories) and 1% BSA (Sigma) for 1 hour then incubated in the primary Abs diluted in blocking solution at room temperature overnight with gentle agitation. After several washes in TBST the secondary Abs were applied in TBST containing 25% of blocking solution for 3 hours. After several washes in TBST, slides were rinsed in DW then sections were mounted in Slowfade Diamond (Invitrogen) and coverslipped. Immunofluorescence was analyzed using a Nikon Eclipse Ti-E inverted microscope (Nikon Instruments Europe B.V., Amsterdam, The Netherlands), with a CFI Plan Apochromat VC 60X oil immersion objective (numerical aperture: 1.4) and an A1R laser confocal system. We used 488 and 647 nm lasers (CVI Melles Griot), and scanning was done in line serial mode, pixel size was 50x50 nm. Image stacks were taken with NIS-Elements AR. For primary and secondary antibodies used in this study, please see Table 1. Quantitative analysis of each dataset was performed by at least two observers, who were blinded to the origin of the samples, the experiments, and did not know of each other's results.

For the quantitative assessment of P2Y12R expression, single high-resolution CLSM image planes were used. Microglial cell bodies, thick (average diameter greater than 1 µm) and thin (average diameter less than 1 µm) processes were identified based on TMEM119 and CX3CR1$^{+/GFP}$ staining. Once the respective outlines of these profiles have been delineated, these outlines have been extended both in the intra- and the extracellular direction with 250-250 nm, yielding a 500 nm wide ribbon-shaped ROI. The integrated fluorescent density of P2Y12R-labeling were measured and divided by the lengths of the respective ROIs, which gave us the P2Y12R fluorescent intensity values applied to unit membrane lengths for each profile.

For the synapse density measurements we used double stainings for pre- and postsynaptic markers (vGluT1 with Homer1 for glutamatergic, and vGAT with Gephyrin for GABAergic synapses). We could validate the specificity and sensitivity of these stainings based on the near-perfect match between pre and postsynaptic markers, thus we continued to measure the presynaptic signals. ROIs were randomly chosen within the neuropil, avoiding cell bodies. The integrated fluorescent densities were measured within these ROIs for vGluT1 and vGAT channels. Measurements were performed with the Fiji software package.

Selective depletion of microglia

CX3CR1$^{+/GFP}$ or C57B1/6J littermates were subjected to 3 weeks of either control or PLX3397 containing diet to create a control and a microglia depleted subgroup of animals, respectively. Extra slices were gathered from each animal by the re-slicing of immersion-fixed or perfusion-fixed acute slice preparations (50 µm). Success of depletion was monitored by creating z-stack images of the native GFP signal of microglia with confocal laser-scanning microscopy, and verified by comparing the total number of microglia counted (via Fiji counting tool) at the same cortical and hippocampal locations, and through the whole depth of the slice preparations.

Patch clamp recordings

Generally accepted guidelines were followed for patching microglial cells (Avignone et al., 2019). After incubation for given timeframes (as specified for each experiments in the Results section), slices were transferred individually into a submerged-type recording chamber with a superfusion system allowing constantly bubbled (95% O2–5% CO2) ACSF to flow at a rate of 3-3.5 ml/min. The ACSF was adjusted to 300-305 mOsm and was constantly saturated with 95% O2–5% CO2 during measurements. All measurements were carried out at 33 –34°C, temperature of ACSF solution was maintained by a dual flow heater (Supertech Instruments). The pipette solution contained (in mM): 120 KCl, 1 CaCl2, 2 MgCl2, 10 HEPES, and 11 EGTA, pH: 7.3, 280-300 mOsm. Pipette resistances were 3-6 MΩ when filled with pipette solution. Visualization of slices and selection of cells (guided by native GFP signal) was done under an upright microscope (BX61WI; Olympus, Tokyo, Japan equipped with infrared-differential interference contrast optics and a UV lamp). Only cells located deeper than ~50 µm measured from the slice surface were targeted. All cells were initially in voltage-clamp mode and held at -40 mV holding potential during the formation of the gigaseal. Series resistance was constantly monitored after the whole-cell configuration was established, and individual recordings taken for analysis showed stability in series resistance between a 5% margin during the whole recording. After whole-cell configuration was established, resting membrane potential values were measured by changing the recording configuration to current-clamp mode at 0 pA for a short period of time (10-15 seconds) and evaluated from the recorded signal via averaging a 5 second period. Thereafter, responses to a pulse-train of current steps (-2 pA to -10 pA with 2 pA increments and 10 ms duration) was recorded. Quantification of input resistance of cells was derived via Ohm's law based on the slope of voltage responses

835 measured at each current steps. The inter-pulse interval was 100 ms. Recordings were
836 performed with a Multiclamp 700B amplifier (Molecular Devices). Data were digitized at 10
837 kHz with a DAQ board (National Instruments, USB-6353) and recorded with a custom
838 software developed in C#.NET and VB.NET in the laboratory. Analysis was done using custom
839 software developed in Delphi and Python environments.

840 ## *LFP Recordings*

841 Acute slice preparations were gathered at each recording day (6 slices/animal, 450 µm
842 thick) in a pairwise manner from control and microglia depleted animals while using the same
843 solutions and equipment. The slice preparation sequence was alternated throughout the
844 recording days between the two groups, as well as the chambers that were used for the
845 incubation process, in order to minimize artefacts that might have been introduced by variance
846 in slice preparation or incubation quality. After at least 1 hour of incubation, slices from both
847 conditions were transferred together in a pairwise manner to a dual perfusion system recording
848 chamber (Hájos and Mody, 2009), and measured simultaneously via performing local field
849 potential (LFP) recordings. In this design, the slices were placed on a metal mesh, and two
850 separate fluid inlets allowed ACSF to flow both above and below the slices at a rate of 3–3.5
851 ml/min for each flow channel at 33 –34°C (Supertech Instruments). Position of slices from the
852 two conditions were also alternated in the recording chamber between subsequent
853 measurements. Standard patch pipettes filled with ACSF were used for LFP recordings. ACSF
854 containing pipette resistances were 3–6 MΩ. In all experiments, electrodes were placed in the
855 hippocampal pyramidal layer of the CA3 region. Recordings were performed with a
856 Multiclamp 700B amplifier (Molecular Devices). Data were digitized at 10 kHz with a DAQ
857 board (National Instruments, USB-6353) and recorded with a software developed in C#.NET
858 and VB.NET in the laboratory.

859 ## *Digital signal processing and analysis*

860 All data were processed and analyzed off-line using self-developed programs written in Delphi
861 6.0 by A.I.G. and Python 2.7.0 by D.S. Signals were filtered with a two-way RC filter to reserve
862 phase. SWRs were pre-detected on 30 Hz low-pass-filtered field recordings using a threshold
863 value of 2-3 times the SD of the signal. Recordings were considered to not contain SWRs if 2
864 times the SD of the signal did not result in detectable events. All automatic detection steps were
865 supervised in each recording. The predetected SWRs were then analyzed using a program that

866 measured various SWR features and eliminates recording artefacts similar to SWRs. Namely,
867 on the low-pass-filtered signal, the program measured: peak amplitude of sharp waves (SWR
868 amplitude); inter- sharp wave interval (SWR rate). On a ripple bandpass-filtered trace (200 ±30
869 Hz), the program also detected the time of negative ripple peaks. Based on this, we identified
870 the ripple cycle closest to the SWR peak and used its negative peak as triggering event for
871 averages to preserve ripple phase. Taking the absolute value of the ripple bandpassed signal
872 and low-pass filtering it, we calculated the ripple power peak (Ripple amplitude). After
873 detection, ~100 consecutive events were selected for quantification, where highest values were
874 measured along the whole recording.

875 ***Quantification and statistical analysis***

876 All quantitative assessment was performed in a blinded manner. Sample size was
877 determined based on sample size calculations performed in our previous experiments using
878 similar models. Data were sampled in a systematic random manner. Experiments were
879 replicated by using multiple animals for slice preparations or histology (biological replicates),
880 and pooled results from experiments were presented in the figures. Exclusion criteria were pre-
881 established for quality of acute slices and immunostainings. No samples had been excluded in
882 the present paper. In the case of two independent groups, Student's t-test or Mann-Whitney U-
883 test, for three or more independent groups Kruskal-Wallis test with Dunn's multiple
884 comparison test was applied. Statistical tests were conducted in custom or self-developed
885 programs in Python environment 2.7.0 by D.S. In this study, data are presented as mean±SEM
886 or in median-Q1-Q3 format, $p<0.05$ was considered statistically significant.

Table 1.

List of antibodies used in the study.

Primary antibodies	host	source	catalog nr.	RRID
Gephyrin	Mouse	Synaptic Systems	147 021	AB_2232546
GFP	Chicken	Invitrogen	A10262	AB_2534023
Homer1	Rabbit	Synaptic Systems	160 003	AB_887730
IBA1	Guinea pig	Synaptic Systems	234004	AB_2493179
Kv2.1	Mouse	NeuroMab	75-014	AB_10673392
P2Y12R	Rabbit	Anaspec	AS-55043A	AB_2298886
TMEM119	Chicken	Synaptic Systems	400 006	AB_2744643
vGAT	Guinea pig	Synaptic Systems	131 004	AB_887873
VGLUT1	Guinea pig	Synaptic Systems	135 304	AB_887878
Secondary antibodies	**host**	**source**	**catalog nr.**	**RRID**
Alexa 488 Streptavidin	-	-	S-11223	-
Alexa 488 anti-chicken	donkey	Jackson ImmunoResearch Labs	703-546-155	AB_2340376
Alexa 488 anti-guinea-pig	donkey	Jackson ImmunoResearch Labs	706-546-148	AB_2340473
Alexa 488 anti-guinea-pig	donkey	Jackson ImmunoResearch Labs	706-546-148	AB_2340473
Alexa 488 anti-mouse	donkey	Thermo Fisher Scientific	A-21202	AB_141607
Alexa 488 anti-rabbit	donkey	Jackson	711-546-152	AB_2340619
Alexa 594 anti-guinea-pig	goat	LifeTech	A11076	AB_141930
Alexa 594 anti-mouse	donkey	Invitrogen	A-21203	AB_141633
Alexa 594 anti-rabbit	donkey	LifeTech	A21207	AB_141637
Alexa 647 anti-chicken	donkey	Jackson ImmunoResearch Labs	703-606-155	AB_2340380
Alexa 647 anti-rabbit	donkey	Jackson ImmunoResearch Labs	711-605-152	AB_2492288
Alexa 647anti-guinnea-pig	donkey	Jackson ImmunoResearch Labs	706-606-148	AB_2340477
Biotinylated anti-chicken	goat	Vector Laboratories	BA-9010	AB_2336114

Additional information

Acknowledgements

We thank László Barna, Pál Vági and the Nikon Imaging Center at the Institute of Experimental Medicine (IEM) for kindly providing microscopy support. We thank Zsolt Kohus for methodological concepts and preliminary electrophysiological data. We are also grateful to Norbert Hájos (IEM), Zoltán Nusser (IEM), István Mody (UCLA) and Dániel Schlingloff (IEM) for their support and useful comments.

Funding

This work was supported by „Momentum" research grant from the Hungarian Academy of Sciences (LP2016-4/2016 to A.D.) ERC-CoG 724994 (to A.D.) and Hungarian Brain Research Program KTIA_13_NAP-A-I/2 (to A.D.). C. C. was supported by the János Bolyai Research Scholarship of the Hungarian Academy of Sciences. C. C. (UNKP-21-5) and B. P. (UNKP-21-4-I) were supported by the New National Excellence Program of the Ministry for Innovation and Technology.

Author contributions

Experimental design and overall concept, A.D., C.C., A.G., P.B.; Methodology, C.C., P.B., B.P., Z.K., E.S.; Formal Analysis C.C., P.B., B.P.; Investigation, P.B., C.C., B.P., E.S., Z.K., A.K., M.N; Resources, A.D., A.G. Writing – Original Draft, P.B.; Editing, P.B., C.C., B.P., A.D., Z.K.; Visualization P.B., C.C., B.P., Z.K. Supervision A.D. and A.G.; Project Administration A.D.; Funding Acquisition, A.D.

Author ORCIDs

Péter Berki: 0000-0001-9550-433X; Csaba Cserép: 0000-0001-5513-2471; Balázs Pósfai: 0000-0003-1035-565X; Eszter Szabadits: 0000-0003-4271-2009; Zsuzsanna Környei: 0000-0001-8281-7994; Anna Kellermayer: 0000-0001-5241-7009; Miklós Nyerges: 0000-0001-5044-6439; Attila I. Gulyás: 0000-0003-4961-636X; Ádám Dénes: 0000-0001-6919-4905.

Competing interests

The authors declare no competing interests.

Ethics statement

All experiments were approved by the Ethical Committee for Animal Research at the Institute of Experimental Medicine, Hungarian Academy of Sciences, and conformed to Hungarian (1998/XXVIII Law on Animal Welfare) and European Communities Council Directive recommendations for the care and use of laboratory animals (2010/63/EU) (license number PE/EA/2552-6/2016; PE/EA/254-7/2019).

Supplementary files

Suppl. Video 1. Time lapse XY (upper) and YZ (lower) views (maximum intensity projections) of a CX3CR1$^{+/GFP}$ microglia moving towards the surface (dotted line) in an acute brain slice. The cell body positions are indicated with coloured dots. Note the extensive process outgrowth and cell body translocation. Scale bar: 10um.

Suppl. Video 2. Time lapse volume view (from YZ view) of a CX3CR1$^{+/GFP}$ microglia with almost stationery cell body, showing still strong process redistribution in an acute brain slice.

925 **Suppl. Video 3.** Morphological changes of individual microglia cells within acute brain slices depicted
926 by maximum intensity projections of XY views. The video starts 1h after slice preparation. Scale bar:
927 10um.

928 **Suppl. Video 4.** Morphological differences of individual microglial cells at different time points during
929 incubation within acute brain slices depicted by 3D reconstructions via morphological analysis tool
930 (Heindl et al., 2018).

931 Data availability

932 Numerical datasets will be available as “Source data files”, uploaded in an editable format.

References

933 Akiyoshi, R., Wake, H., Kato, D., Horiuchi, H., Ono, R., Ikegami, A., Haruwaka, K., Omori, T.,
934 Tachibana, Y., Moorhouse, A. J., & Nabekura, J. (2018). Microglia Enhance Synapse
935 Activity to Promote Local Network Synchronization. *ENeuro*, *5*(5), ENEURO.0088-18.2018.
936 https://doi.org/10.1523/ENEURO.0088-18.2018
937 Andersen, P. (1981). Brain slices—A neurobiological tool of increasing usefulness. *Trends in*
938 *Neurosciences*, *4*, 53–56. https://doi.org/10.1016/0166-2236(81)90019-9
939 Avignone, E., Milior, G., Arnoux, I., & Audinat, E. (2019). *Electrophysiological Investigation of*
940 *Microglia* (Vol. 2034, p. 111). Springer. https://doi.org/10.1007/978-1-4939-9658-2_9
941 Basilico, B., Ferrucci, L., Ratano, P., Golia, M. T., Grimaldi, A., Rosito, M., Ferretti, V., Reverte, I.,
942 Sanchini, C., Marrone, M. C., Giubettini, M., De Turris, V., Salerno, D., Garofalo, S., St-
943 Pierre, M.-K., Carrier, M., Renzi, M., Pagani, F., Modi, B., … Ragozzino, D. (2022).
944 Microglia control glutamatergic synapses in the adult mouse hippocampus. *Glia*, *70*(1), 173–
945 195. https://doi.org/10.1002/glia.24101
946 Bennett, F. C., Bennett, M. L., Yaqoob, F., Mulinyawe, S. B., Grant, G. A., Hayden Gephart, M.,
947 Plowey, E. D., & Barres, B. A. (2018). A Combination of Ontogeny and CNS Environment
948 Establishes Microglial Identity. *Neuron*, *98*(6), 1170-1183.e8.
949 https://doi.org/10.1016/j.neuron.2018.05.014
950 Bohlen, C. J., Bennett, F. C., Tucker, A. F., Collins, H. Y., Mulinyawe, S. B., & Barres, B. A. (2017).
951 Diverse Requirements for Microglial Survival, Specification, and Function Revealed by
952 Defined-Medium Cultures. *Neuron*, *94*(4), 759-773.e8.
953 https://doi.org/10.1016/j.neuron.2017.04.043
954 Bosco, D. B., Zheng, J., Xu, Z., Peng, J., Eyo, U. B., Tang, K., Yan, C., Huang, J., Feng, L., Wu, G.,
955 Richardson, J. R., Wang, H., & Wu, L.-J. (2018). RNAseq analysis of hippocampal microglia
956 after kainic acid-induced seizures. *Molecular Brain*, *11*(1), 34.
957 https://doi.org/10.1186/s13041-018-0376-5

Boucsein, C., Kettenmann, H., & Nolte, C. (2000). Electrophysiological properties of microglial cells in normal and pathologic rat brain slices. *European Journal of Neuroscience*, *12*(6), 2049–2058. https://doi.org/10.1046/j.1460-9568.2000.00100.x

Boucsein, C., Zacharias, R., Färber, K., Pavlovic, S., Hanisch, U.-K., & Kettenmann, H. (2003). Purinergic receptors on microglial cells: Functional expression in acute brain slices and modulation of microglial activation in vitro. *European Journal of Neuroscience*, *17*(11), 2267–2276. https://doi.org/10.1046/j.1460-9568.2003.02663.x

Bourne, J. N., Kirov, S. A., Sorra, K. E., & Harris, K. M. (2007). Warmer preparation of hippocampal slices prevents synapse proliferation that might obscure LTP-related structural plasticity. *Neuropharmacology*, *52*(1), 55–59. https://doi.org/10.1016/j.neuropharm.2006.06.020

Brahma, B., Forman, R. e., Stewart, E. e., Nicholson, C., & Rice, M. e. (2000). Ascorbate Inhibits Edema in Brain Slices. *Journal of Neurochemistry*, *74*(3), 1263–1270. https://doi.org/10.1046/j.1471-4159.2000.741263.x

Butovsky, O., Jedrychowski, M. P., Moore, C. S., Cialic, R., Lanser, A. J., Gabriely, G., Koeglsperger, T., Dake, B., Wu, P. M., Doykan, C. E., Fanek, Z., Liu, L., Chen, Z., Rothstein, J. D., Ransohoff, R. M., Gygi, S. P., Antel, J. P., & Weiner, H. L. (2014). Identification of a unique TGF-β–dependent molecular and functional signature in microglia. *Nature Neuroscience*, *17*(1), 131–143. https://doi.org/10.1038/nn.3599

Cserép, C., Pósfai, B., Lénárt, N., Fekete, R., László, Z. I., Lele, Z., Orsolits, B., Molnár, G., Heindl, S., Schwarcz, A. D., Ujvári, K., Környei, Z., Tóth, K., Szabadits, E., Sperlágh, B., Baranyi, M., Csiba, L., Hortobágyi, T., Maglóczky, Z., … Dénes, Á. (2020). Microglia monitor and protect neuronal function through specialized somatic purinergic junctions. *Science*. https://doi.org/10.1126/science.aax6752

Davalos, D., Grutzendler, J., Yang, G., Kim, J. V., Zuo, Y., Jung, S., Littman, D. R., Dustin, M. L., & Gan, W.-B. (2005). ATP mediates rapid microglial response to local brain injury in vivo. *Nature Neuroscience*, *8*(6), 752–758. https://doi.org/10.1038/nn1472

984 Davies, D. S., Ma, J., Jegathees, T., & Goldsbury, C. (2017). Microglia show altered morphology and
985 reduced arborization in human brain during aging and Alzheimer's disease. *Brain Pathology*,
986 *27*(6), 795–808. https://doi.org/10.1111/bpa.12456
987 Dissing-Olesen, L., LeDue, J. M., Rungta, R. L., Hefendehl, J. K., Choi, H. B., & MacVicar, B. A.
988 (2014). Activation of Neuronal NMDA Receptors Triggers Transient ATP-Mediated
989 Microglial Process Outgrowth. *Journal of Neuroscience*, *34*(32), 10511–10527.
990 https://doi.org/10.1523/JNEUROSCI.0405-14.2014
991 Eguchi, K., Velicky, P., Hollergschwandtner, E., Itakura, M., Fukazawa, Y., Danzl, J. G., &
992 Shigemoto, R. (2020). Advantages of Acute Brain Slices Prepared at Physiological
993 Temperature in the Characterization of Synaptic Functions. *Frontiers in Cellular*
994 *Neuroscience*, *14*, 63. https://doi.org/10.3389/fncel.2020.00063
995 Elmore, M. R. P., Najafi, A. R., Koike, M. A., Dagher, N. N., Spangenberg, E. E., Rice, R. A.,
996 Kitazawa, M., Matusow, B., Nguyen, H., West, B. L., & Green, K. N. (2014). Colony-
997 Stimulating Factor 1 Receptor Signaling Is Necessary for Microglia Viability, Unmasking a
998 Microglia Progenitor Cell in the Adult Brain. *Neuron*, *82*(2), 380–397.
999 https://doi.org/10.1016/j.neuron.2014.02.040
1000 Eyo, U. B., Peng, J., Swiatkowski, P., Mukherjee, A., Bispo, A., & Wu, L.-J. (2014). Neuronal
1001 Hyperactivity Recruits Microglial Processes via Neuronal NMDA Receptors and Microglial
1002 P2Y12 Receptors after Status Epilepticus. *Journal of Neuroscience*, *34*(32), 10528–10540.
1003 https://doi.org/10.1523/JNEUROSCI.0416-14.2014
1004 Eyo, U. B., & Wu, L.-J. (2013). Bidirectional Microglia-Neuron Communication in the Healthy
1005 Brain. *Neural Plasticity*, *2013*, e456857. https://doi.org/10.1155/2013/456857
1006 Färber, K., & Kettenmann, H. (2005). Physiology of microglial cells. *Brain Research Reviews*, *48*(2),
1007 133–143. https://doi.org/10.1016/j.brainresrev.2004.12.003
1008 Gosselin, D., Skola, D., Coufal, N., Holtman, I., Schlachetzki, J., Sajti, E., Jaeger, B., O'Connor, C.,
1009 Fitzpatrick, C., Pasillas, M., Pena, M., Adair, A., Gonda, D., Levy, M., Ransohoff, R., Gage,
1010 F., & Glass, C. (2017). An environment-dependent transcriptional network specifies human
1011 microglia identity. *Science (New York, N.Y.)*, *356*. https://doi.org/10.1126/science.aal3222

1012 Gu, N., Eyo, U. B., Murugan, M., Peng, J., Matta, S., Dong, H., & Wu, L.-J. (2016). Microglial
1013 P2Y12 receptors regulate microglial activation and surveillance during neuropathic pain.
1014 *Brain, Behavior, and Immunity*, *55*, 82–92. https://doi.org/10.1016/j.bbi.2015.11.007
1015 Hájos, N., Ellender, T. J., Zemankovics, R., Mann, E. O., Exley, R., Cragg, S. J., Freund, T. F., &
1016 Paulsen, O. (2009). Maintaining network activity in submerged hippocampal slices:
1017 Importance of oxygen supply. *European Journal of Neuroscience*, *29*(2), 319–327.
1018 https://doi.org/10.1111/j.1460-9568.2008.06577.x
1019 Hájos, N., Karlócai, M. R., Németh, B., Ulbert, I., Monyer, H., Szabó, G., Erdélyi, F., Freund, T. F.,
1020 & Gulyás, A. I. (2013). Input-output features of anatomically identified CA3 neurons during
1021 hippocampal sharp wave/ripple oscillation in vitro. *Journal of Neuroscience*, *33*(28), 11677–
1022 11691.
1023 Hájos, N., & Mody, I. (2009). Establishing a physiological environment for visualized in vitro brain
1024 slice recordings by increasing oxygen supply and modifying aCSF content. *Journal of*
1025 *Neuroscience Methods*, *183*(2), 107–113.
1026 Han, J., Harris, R. A., & Zhang, X.-M. (2017). An updated assessment of microglia depletion: Current
1027 concepts and future directions. *Molecular Brain*, *10*, 25. https://doi.org/10.1186/s13041-017-
1028 0307-x
1029 Haynes, S. E., Hollopeter, G., Yang, G., Kurpius, D., Dailey, M. E., Gan, W.-B., & Julius, D. (2006).
1030 The P2Y12 receptor regulates microglial activation by extracellular nucleotides. *Nature*
1031 *Neuroscience*, *9*(12), 1512–1519. https://doi.org/10.1038/nn1805
1032 Heindl, S., Gesierich, B., Benakis, C., Llovera, G., Duering, M., & Liesz, A. (2018). Automated
1033 Morphological Analysis of Microglia After Stroke. *Frontiers in Cellular Neuroscience*, *12*,
1034 106. https://doi.org/10.3389/fncel.2018.00106
1035 Hellwig, S., Heinrich, A., & Biber, K. (2013). The brain's best friend: Microglial neurotoxicity
1036 revisited. *Frontiers in Cellular Neuroscience*, *7*.
1037 https://www.frontiersin.org/article/10.3389/fncel.2013.00071

1038 Hickman, S. E., Kingery, N. D., Ohsumi, T. K., Borowsky, M. L., Wang, L., Means, T. K., & El
1039 Khoury, J. (2013). The microglial sensome revealed by direct RNA sequencing. *Nature*
1040 *Neuroscience*, *16*(12), 1896–1905. https://doi.org/10.1038/nn.3554
1041 Hirbec, H., Rassendren, F., & Audinat, E. (2019). Microglia Reactivity: Heterogeneous Pathological
1042 Phenotypes. In O. Garaschuk & A. Verkhratsky (Eds.), *Microglia: Methods and Protocols*
1043 (pp. 41–55). Springer. https://doi.org/10.1007/978-1-4939-9658-2_4
1044 Holderith, N., Heredi, J., Kis, V., & Nusser, Z. (2020). A High-Resolution Method for Quantitative
1045 Molecular Analysis of Functionally Characterized Individual Synapses. *Cell Reports*, *32*(4),
1046 107968. https://doi.org/10.1016/j.celrep.2020.107968
1047 Holtman, I. R., Raj, D. D., Miller, J. A., Schaafsma, W., Yin, Z., Brouwer, N., Wes, P. D., Möller, T.,
1048 Orre, M., Kamphuis, W., Hol, E. M., Boddeke, E. W. G. M., & Eggen, B. J. L. (2015).
1049 Induction of a common microglia gene expression signature by aging and neurodegenerative
1050 conditions: A co-expression meta-analysis. *Acta Neuropathologica Communications*, *3*(1),
1051 31. https://doi.org/10.1186/s40478-015-0203-5
1052 Huchzermeyer, C., Berndt, N., Holzhütter, H.-G., & Kann, O. (2013). Oxygen Consumption Rates
1053 during Three Different Neuronal Activity States in the Hippocampal CA3 Network. *Journal*
1054 *of Cerebral Blood Flow & Metabolism*, *33*(2), 263–271.
1055 https://doi.org/10.1038/jcbfm.2012.165
1056 Ikegami, A., Haruwaka, K., & Wake, H. (2019). Microglia: Lifelong modulator of neural circuits.
1057 *Neuropathology*, *39*(3), 173–180. https://doi.org/10.1111/neup.12560
1058 Ivanov, A., & Zilberter, Y. (2011). Critical State of Energy Metabolism in Brain Slices: The Principal
1059 Role of Oxygen Delivery and Energy Substrates in Shaping Neuronal Activity. *Frontiers in*
1060 *Neuroenergetics*, *3*, 9. https://doi.org/10.3389/fnene.2011.00009
1061 Izquierdo, P., Attwell, D., & Madry, C. (2019). Ion Channels and Receptors as Determinants of
1062 Microglial Function. *Trends in Neurosciences*, *42*(4), 278–292.
1063 https://doi.org/10.1016/j.tins.2018.12.007
1064 Kato, G., Inada, H., Wake, H., Akiyoshi, R., Miyamoto, A., Eto, K., Ishikawa, T., Moorhouse, A. J.,
1065 Strassman, A. M., & Nabekura, J. (2016). Microglial Contact Prevents Excess Depolarization

and Rescues Neurons from Excitotoxicity. *ENeuro*, *3*(3), ENEURO.0004-16.2016. https://doi.org/10.1523/ENEURO.0004-16.2016

Kettenmann, H., Hanisch, U.-K., Noda, M., & Verkhratsky, A. (2011). Physiology of Microglia. *Physiological Reviews*, *91*(2), 461–553. https://doi.org/10.1152/physrev.00011.2010

Kierdorf, K., & Prinz, M. (2017). Microglia in steady state. *The Journal of Clinical Investigation*, *127*(9), 3201–3209. https://doi.org/10.1172/JCI90602

Kirov, S. A., Sorra, K. E., & Harris, K. M. (1999). Slices Have More Synapses than Perfusion-Fixed Hippocampus from both Young and Mature Rats. *Journal of Neuroscience*, *19*(8), 2876–2886. https://doi.org/10.1523/JNEUROSCI.19-08-02876.1999

Koshinaga, M., Katayama, Y., Fukushima, M., Oshima, H., Suma, T., & Takahata, T. (2000). Rapid and Widespread Microglial Activation Induced by Traumatic Brain Injury in Rat Brain Slices. *Journal of Neurotrauma*, *17*(3), 185–192. https://doi.org/10.1089/neu.2000.17.185

Lin, S.-S., Tang, Y., Illes, P., & Verkhratsky, A. (2021). The Safeguarding Microglia: Central Role for P2Y12 Receptors. *Frontiers in Pharmacology*, *11*, 2218. https://doi.org/10.3389/fphar.2020.627760

Liu, Y.-J., Green, K. N., Holmes, T. C., & Xu, X. (2022). Commentary: How Do Microglia Regulate Neural Circuit Connectivity and Activity in the Adult Brain? *Neuroscience Insights*, *17*, 26331055211071124. https://doi.org/10.1177/26331055211071124

Liu, Y.-J., Spangenberg, E. E., Tang, B., Holmes, T. C., Green, K. N., & Xu, X. (2021). Microglia Elimination Increases Neural Circuit Connectivity and Activity in Adult Mouse Cortex. *Journal of Neuroscience*, *41*(6), 1274–1287. https://doi.org/10.1523/JNEUROSCI.2140-20.2020

Madry, C., Arancibia-Cárcamo, I. L., Kyrargyri, V., Chan, V. T. T., Hamilton, N. B., & Attwell, D. (2018). Effects of the ecto-ATPase apyrase on microglial ramification and surveillance reflect cell depolarization, not ATP depletion. *Proceedings of the National Academy of Sciences*, *115*(7), E1608–E1617. https://doi.org/10.1073/pnas.1715354115

Madry, C., Kyrargyri, V., Arancibia-Cárcamo, I. L., Jolivet, R., Kohsaka, S., Bryan, R. M., & Attwell, D. (2018). Microglial Ramification, Surveillance, and Interleukin-1β Release Are Regulated

by the Two-Pore Domain K+ Channel THIK-1. *Neuron*, *97*(2), 299-312.e6. https://doi.org/10.1016/j.neuron.2017.12.002

Mann, E. O., Suckling, J. M., Hajos, N., Greenfield, S. A., & Paulsen, O. (2005). Perisomatic Feedback Inhibition Underlies Cholinergically Induced Fast Network Oscillations in the Rat Hippocampus In Vitro. *Neuron*, *45*(1), 105–117. https://doi.org/10.1016/j.neuron.2004.12.016

Masuda, T., Sankowski, R., Staszewski, O., & Prinz, M. (2020). Microglia Heterogeneity in the Single-Cell Era. *Cell Reports*, *30*(5), 1271–1281. https://doi.org/10.1016/j.celrep.2020.01.010

Matyash, M., Zabiegalov, O., Wendt, S., Matyash, V., & Kettenmann, H. (2017). The adenosine generating enzymes CD39/CD73 control microglial processes ramification in the mouse brain. *PLOS ONE*, *12*(4), e0175012. https://doi.org/10.1371/journal.pone.0175012

Melief, J., Koning, N., Schuurman, K. G., Van De Garde, M. D. B., Smolders, J., Hoek, R. M., Van Eijk, M., Hamann, J., & Huitinga, I. (2012). Phenotyping primary human microglia: Tight regulation of LPS responsiveness. *Glia*, *60*(10), 1506–1517. https://doi.org/10.1002/glia.22370

Mildner, A., Huang, H., Radke, J., Stenzel, W., & Priller, J. (2017). P2Y12 receptor is expressed on human microglia under physiological conditions throughout development and is sensitive to neuroinflammatory diseases. *Glia*, *65*(2), 375–387. https://doi.org/10.1002/glia.23097

Miyamoto, A., Wake, H., Ishikawa, A. W., Eto, K., Shibata, K., Murakoshi, H., Koizumi, S., Moorhouse, A. J., Yoshimura, Y., & Nabekura, J. (2016). Microglia contact induces synapse formation in developing somatosensory cortex. *Nature Communications*, *7*(1), 12540. https://doi.org/10.1038/ncomms12540

Miyamoto, A., Wake, H., Moorhouse, A., & Nabekura, J. (2013). Microglia and synapse interactions: Fine tuning neural circuits and candidate molecules. *Frontiers in Cellular Neuroscience*, *7*, 70. https://doi.org/10.3389/fncel.2013.00070

Morrison, H. W., & Filosa, J. A. (2013). A quantitative spatiotemporal analysis of microglia morphology during ischemic stroke and reperfusion. *Journal of Neuroinflammation*, *10*(1), 782. https://doi.org/10.1186/1742-2094-10-4

1121 Mulkey, D. K., Henderson, R. A., Olson, J. E., Putnam, R. W., & Dean, J. B. (2001). Oxygen
1122 measurements in brain stem slices exposed to normobaric hyperoxia and hyperbaric oxygen.
1123 *Journal of Applied Physiology*, *90*(5), 1887–1899.
1124 https://doi.org/10.1152/jappl.2001.90.5.1887
1125 Nasu-Tada, K., Koizumi, S., & Inoue, K. (2005). Involvement of β1 integrin in microglial chemotaxis
1126 and proliferation on fibronectin: Different regulations by ADP through PKA. *Glia*, *52*(2), 98–
1127 107. https://doi.org/10.1002/glia.20224
1128 Nimmerjahn, A., Kirchhoff, F., & Helmchen, F. (2005). Resting Microglial Cells Are Highly
1129 Dynamic Surveillants of Brain Parenchyma in Vivo. *Science*.
1130 https://doi.org/10.1126/science.1110647
1131 Pannasch, U., & Rouach, N. (2013). Emerging role for astroglial networks in information processing:
1132 From synapse to behavior. *Trends in Neurosciences*, *36*(7), 405–417.
1133 https://doi.org/10.1016/j.tins.2013.04.004
1134 Peng, J., Liu, Y., Umpierre, A. D., Xie, M., Tian, D.-S., Richardson, J. R., & Wu, L.-J. (2019).
1135 Microglial P2Y12 receptor regulates ventral hippocampal CA1 neuronal excitability and
1136 innate fear in mice. *Molecular Brain*, *12*(1), 71. https://doi.org/10.1186/s13041-019-0492-x
1137 Perumal, M. B., Latimer, B., Xu, L., Stratton, P., Nair, S., & Sah, P. (2021). Microcircuit mechanisms
1138 for the generation of sharp-wave ripples in the basolateral amygdala: A role for chandelier
1139 interneurons. *Cell Reports*, *35*(6), 109106. https://doi.org/10.1016/j.celrep.2021.109106
1140 Petersen, M. A., & Dailey, M. E. (2004). Diverse microglial motility behaviors during clearance of
1141 dead cells in hippocampal slices. *Glia*, *46*(2), 195–206. https://doi.org/10.1002/glia.10362
1142 Prinz, M., Jung, S., & Priller, J. (2019). Microglia Biology: One Century of Evolving Concepts. *Cell*,
1143 *179*(2), 292–311. https://doi.org/10.1016/j.cell.2019.08.053
1144 Richerson, G. B., & Messer, C. (1995). Effect of composition of experimental solutions on neuronal
1145 survival during rat brain slicing. *Experimental Neurology*, *131*(1), 133–143.
1146 https://doi.org/10.1016/0014-4886(95)90015-2
1147 Sadler, R., Cramer, J. V., Heindl, S., Kostidis, S., Betz, D., Zuurbier, K. R., Northoff, B. H., Heijink,
1148 M., Goldberg, M. P., Plautz, E. J., Roth, S., Malik, R., Dichgans, M., Holdt, L. M., Benakis,

1149 C., Giera, M., Stowe, A. M., & Liesz, A. (2020). Short-Chain Fatty Acids Improve Poststroke
1150 Recovery via Immunological Mechanisms. *Journal of Neuroscience*, *40*(5), 1162–1173.
1151 https://doi.org/10.1523/JNEUROSCI.1359-19.2019
1152 Salter, M. W., & Stevens, B. (2017). Microglia emerge as central players in brain disease. *Nature*
1153 *Medicine*, *23*(9), 1018–1027. https://doi.org/10.1038/nm.4397
1154 Savage, J. C., Carrier, M., & Tremblay, M.-È. (2019). Morphology of Microglia Across Contexts of
1155 Health and Disease. In O. Garaschuk & A. Verkhratsky (Eds.), *Microglia: Methods and*
1156 *Protocols* (pp. 13–26). Springer. https://doi.org/10.1007/978-1-4939-9658-2_2
1157 Schilling, T., & Eder, C. (2007a). Ion channel expression in resting and activated microglia of
1158 hippocampal slices from juvenile mice. *Brain Research*, *1186*, 21–28.
1159 https://doi.org/10.1016/j.brainres.2007.10.027
1160 Schilling, T., & Eder, C. (2007b). Ion channel expression in resting and activated microglia of
1161 hippocampal slices from juvenile mice. *Brain Research*, *1186*, 21–28.
1162 https://doi.org/10.1016/j.brainres.2007.10.027
1163 Schilling, T., Quandt, F. N., Cherny, V. V., Zhou, W., Heinemann, U., Decoursey, T. E., & Eder, C.
1164 (2000). Upregulation of Kv1.3 K+ channels in microglia deactivated by TGF-β. *American*
1165 *Journal of Physiology-Cell Physiology*, *279*(4), C1123–C1134.
1166 https://doi.org/10.1152/ajpcell.2000.279.4.C1123
1167 Schlingloff, D., Káli, S., Freund, T. F., Hájos, N., & Gulyás, A. I. (2014). Mechanisms of sharp wave
1168 initiation and ripple generation. *Journal of Neuroscience*, *34*(34), 11385–11398.
1169 Schmid, C. D., Melchior, B., Masek, K., Puntambekar, S. S., Danielson, P. E., Lo, D. D., Gregor
1170 Sutcliffe, J., & Carson, M. J. (2009). Differential gene expression in LPS/IFNγ activated
1171 microglia and macrophages: In vitro versus in vivo. *Journal of Neurochemistry*, *109*(s1), 117–
1172 125. https://doi.org/10.1111/j.1471-4159.2009.05984.x
1173 Singh, V., Sadler, R., Heindl, S., Llovera, G., Roth, S., Benakis, C., & Liesz, A. (2018). The gut
1174 microbiome primes a cerebroprotective immune response after stroke. *Journal of Cerebral*
1175 *Blood Flow & Metabolism*, *38*(8), 1293–1298. https://doi.org/10.1177/0271678X18780130

1176 Sipe, G. O., Lowery, Tremblay, M.-È., Kelly, E. A., Lamantia, C. E., & Majewska, A. K. (2016).
1177 Microglial P2Y12 is necessary for synaptic plasticity in mouse visual cortex. *Nature*
1178 *Communications*, *7*(1), 10905. https://doi.org/10.1038/ncomms10905
1179 Song, W. M., & Colonna, M. (2018). Chapter One—The Microglial Response to Neurodegenerative
1180 Disease. In F. Alt (Ed.), *Advances in Immunology* (Vol. 139, pp. 1–50). Academic Press.
1181 https://doi.org/10.1016/bs.ai.2018.04.002
1182 Stence, N., Waite, M., & Dailey, M. E. (2001). Dynamics of microglial activation: A confocal time-
1183 lapse analysis in hippocampal slices. *Glia*, *33*(3), 256–266. https://doi.org/10.1002/1098-
1184 1136(200103)33:3<256::AID-GLIA1024>3.0.CO;2-J
1185 Strackeljan, L., Baczynska, E., Cangalaya, C., Baidoe-Ansah, D., Wlodarczyk, J., Kaushik, R., &
1186 Dityatev, A. (2021). Microglia Depletion-Induced Remodeling of Extracellular Matrix and
1187 Excitatory Synapses in the Hippocampus of Adult Mice. *Cells*, *10*(8), 1862.
1188 https://doi.org/10.3390/cells10081862
1189 Swiatkowski, P., Murugan, M., Eyo, U. B., Wang, Y., Rangaraju, S., Oh, S. B., & Wu, L.-J. (2016).
1190 Activation of microglial P2Y12 receptor is required for outward potassium currents in
1191 response to neuronal injury. *Neuroscience*, *318*, 22–33.
1192 https://doi.org/10.1016/j.neuroscience.2016.01.008
1193 Thion, M. S., Ginhoux, F., & Garel, S. (2018). Microglia and early brain development: An intimate
1194 journey. *Science (New York, N.Y.)*, *362*(6411), 185–189.
1195 https://doi.org/10.1126/science.aat0474
1196 Ting, J. T., Daigle, T. L., Chen, Q., & Feng, G. (2014). Acute Brain Slice Methods for Adult and
1197 Aging Animals: Application of Targeted Patch Clamp Analysis and Optogenetics. In M.
1198 Martina & S. Taverna (Eds.), *Patch-Clamp Methods and Protocols* (pp. 221–242). Springer.
1199 https://doi.org/10.1007/978-1-4939-1096-0_14
1200 Tóth, K., Lénárt, N., Berki, P., Fekete, R., Szabadits, E., Pósfai, B., Cserép, C., Alatshan, A., Benkő,
1201 S., Kiss, D., Hübner, C. A., Gulyás, A., Kaila, K., Környei, Z., & Dénes, Á. (2022). The
1202 NKCC1 ion transporter modulates microglial phenotype and inflammatory response to brain

injury in a cell-autonomous manner. *PLOS Biology*, *20*(1), e3001526. https://doi.org/10.1371/journal.pbio.3001526

Trivino-Paredes, J. S., Nahirney, P. C., Pinar, C., Grandes, P., & Christie, B. R. (2019). Acute slice preparation for electrophysiology increases spine numbers equivalently in the male and female juvenile hippocampus: A DiI labeling study. *Journal of Neurophysiology*, *122*(3), 958–969. https://doi.org/10.1152/jn.00332.2019

Verkhratsky, A., & Nedergaard, M. (2018). Physiology of Astroglia. *Physiological Reviews*, *98*(1), 239–389. https://doi.org/10.1152/physrev.00042.2016

Wang, S., & Colonna, M. (2019). Microglia in Alzheimer's disease: A target for immunotherapy. *Journal of Leukocyte Biology*, *106*(1), 219–227. https://doi.org/10.1002/JLB.MR0818-319R

Wu, C., Luk, W. P., Gillis, J., Skinner, F., & Zhang, L. (2005). Size Does Matter: Generation of Intrinsic Network Rhythms in Thick Mouse Hippocampal Slices. *Journal of Neurophysiology*, *93*(4), 2302–2317. https://doi.org/10.1152/jn.00806.2004

Yamamoto, C., & McIlwain, H. (1966). Electrical Activities in Thin Sections from the Mammalian Brain Maintained in Chemically-Defined Media in Vitro. *Journal of Neurochemistry*, *13*(12), 1333–1343. https://doi.org/10.1111/j.1471-4159.1966.tb04296.x

Zrzavy, T., Hametner, S., Wimmer, I., Butovsky, O., Weiner, H. L., & Lassmann, H. (2017). Loss of 'homeostatic' microglia and patterns of their activation in active multiple sclerosis. *Brain*, *140*(7), 1900–1913. https://doi.org/10.1093/brain/awx113